OSCILLATORS: RESONANCES AND EXCITATIONS

A Dissertation

presented to

the Faculty of the Graduate School

University of Missouri

In Partial Fulfillment

of the Requirements for the Degree

Doctor of Philosophy

---

by

K.R. FELTS

Dr. Carmen Chicone, Dissertation Supervisor

MAY 2009

The undersigned, appointed by the Dean of the Graduate School, have examined the dissertation entitled

OSCILLATORS: RESONANCES AND EXCITATIONS

presented by K.R. Felts,

a candidate for the degree of Doctor of Philosophy of Mathematics and hereby certify that in their opinion it is worthy of acceptance.

Professor Carmen Chicone

Professor Loukas Grafakos

Professor Yuri Latushkin

Professor Marius Mitrea

Professor Bahram Mashhoon

DEDICATION

This dissertation is dedicated to everyone that has helped me succeed. I would like to personally thank Dr. Carmen Chicone for sticking with me for eight years and all the assistance provided while researching and writing. My thanks go out to Columbia College for the chance to begin my career as a faculty member while I continued pursuit of my degree. I thank the many friends I've made throughout life, both in my younger years and during my time at the university, you have all helped shape my path. I also wish to thank my family, especially my parents, for the love and support provided for the past thirty-one years.

Finally, I dedicate this dissertation to the two most important people in my life, my beautiful and supportive wife and our amazing son. I can't imagine my life without either of you, my love for goes beyond mere words. To my wife, this document is evidence of the unconditional love, patience, and understanding you have given me during our years together, I thank you for being you.

ACKNOWLEDGEMENTS

Thanks to my committee members Dr. Carmen Chicone, Dr. Loukas Grafakos, Dr. Bahram Mashhoon, Dr. Marius Mitrea, and Dr. Yuri Latushkin for their time and assistance. Thanks to Dr. Brian Mann for presenting the impact oscillator problem and for the data supplied. I would also like to thank the many other faculty and staff in the University of Missouri mathematics department that have helped me throughout my research.

Table of Contents

List of Figures

List of Tables

Chapter 1

Introduction

This thesis is a compilation of work done in the field of oscillators. One topic is an investigation into impact oscillators and their properties. The second topic is concerned with excitation of oscillators. The thesis begins with mathematical preliminaries; this chapter will explain Hertzian contact and Melnikov theory. The next chapter investigates a mathematical model utilizing Hertzian contact to predict the behavior of a steel pendulum bob striking an aluminum alloy barrier. The model is shown to capture the qualitative and quantitative behavior of the impact oscillator and demonstrates a new qualitative effect: Existence of a non-monotone period function. The following chapter will prove the existence of a non-monotone period function for more general impact oscillators. The final chapter is devoted to excitation of energy in periodic or nearly periodic classical Hamiltonian systems.

Chapter 2

Preliminaries

2.1 Hertzian Contact

Hertzian contact describes a method for finding the displacement in surfaces when two elastic solids collide. The formulation of Hertzian contact used in later chapters is concerned with the displacement caused by a sphere impacting the plane, so the overview in this chapter will only be concerned with sphere-to-plane contact. We assume that the sphere is rigid. This approximation is valid as our experiments involve a steel bob impacting an aluminum surface. The elastic modulus of steel is much greater than aluminum, hence the displacement of points on the sphere's surface will be negligible compared to the displacement of points on the planar surface. Finally, we assume the depth of penetration of the sphere will be small compared to the radius of the sphere. For more information on the derivation of Hertzian contact (or other contact mechanics) the reader is referred to [9, 13].

The surfaces of the sphere of radius R ($z = R - \sqrt{R^2 - x^2 - y^2}$) and plane ($z = 0$) near the point of initial contact (taken to be the origin) are denoted by S_1 and S_2 respectively. The contact region that results when the sphere impacts the plane will be circular. Let a be the radius of the contact region and $A := \{(x, y) | \, x^2 + y^2 \leq a^2\}$. As

the contact region is circular, it will be beneficial to represent points in the contact region in polar coordinates. The key element of Hertzian contact comes with the choice of how to define the pressure distribution at each point in the contact region. Hertzian contact utilizes a pressure distribution, in polar coordinates (r, θ), of the form $p(r) := \frac{p_0}{a}\sqrt{a^2 - r^2} = p_0\sqrt{1 - (r/a)^2}$, $0 \leq r \leq a$, where p_0 is the pressure along the z-axis.

We define the normal (tangent to the z-axis) displacement at a point (x, y) on the displaced surface S by $u_S(\sqrt{x^2 + y^2})$. Using a result of general contact mechanics (see [13]), the normal displacement at a point (x, y) in the contact region is given by

$$u_S(\sqrt{x^2 + y^2}) = \frac{1 - \nu^2}{\pi E} \int\int_A \frac{p(\sqrt{\bar{x}^2 + \bar{y}^2})}{\sqrt{(\bar{x} - x)^2 + (\bar{y} - y)^2}}\, d\bar{x} d\bar{y}$$

where the constants ν, Poisson's ratio, and E, Young's modulus, are determined by the physical nature of each solid. Poisson's ratio is the ratio of the transverse strain to the axial strain where the axis is along the direction that the force is applied. The range of Poisson's ratio is $-1 \leq \nu \leq 0.5$, although for most materials $0 \leq \nu \leq 0.5$. Young's modulus, also known as the elastic modulus, is the ratio of stress to strain for the range of stresses in which Hooke's Law holds. Using the polar change of variables $\bar{x} = x + s\cos(w)$, $\bar{y} = y + s\sin(w)$, the normal displacement can be rewritten as

$$u_S(r) = \frac{1 - \nu^2}{\pi E} \int_0^{2\pi} \int_0^{s_1} p(t)\, ds\, dw \tag{2.1}$$

where $r = \sqrt{x^2 + y^2}$ and the relationship between s, w, t, r and s_1 in the contact region is shown in Fig. 2.1.

Using the Law of Cosines and the definition of the Hertzian pressure distribution,

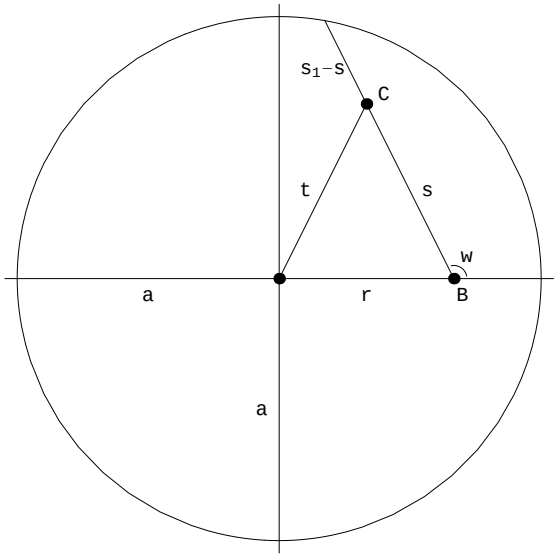

Figure 2.1: An illustration of the contact region. The points B and C have cartesian coordinates (x, y) and $(\bar{x}, \bar{y})$ respectively (for simplicity of the figure, we have shown $y = 0$). The distance from the origin to point B is r and the distance from the origin to point C is t. The distance from point B to point C is denoted by s with corresponding angle w. The quantity s_1 is the distance from point B to the boundary along the direction given by w.

$t^2 = r^2 + s^2 + 2rs\cos w$ and we can express equation (2.1) as

$$u_S(r) = \big(\frac{1-\nu^2}{\pi E}\big)\big(\frac{p_0}{a}\big)\int_0^{2\pi}\int_0^{s_1}\sqrt{(\alpha^2+\beta^2)-(s+\beta)^2}\,ds\,dw$$

where $\alpha^2 = a^2 - r^2$ and $\beta = r\cos w$. Integration in s yields

$$\begin{aligned} u_S(r) &= \big(\frac{1-\nu^2}{\pi E}\big)\big(\frac{p_0}{a}\big)\int_0^{2\pi}\frac{\alpha^2+\beta^2}{2}\big(\frac{\pi}{2}-\arctan\big(\frac{\beta}{\alpha}\big)\big)-\frac{1}{2}\beta\alpha\,dw \\ &= \big(\frac{1-\nu^2}{E}\big)\big(\frac{p_0}{4a}\big)\int_0^{2\pi}\alpha^2+\beta^2\,dw \\ &= \big(\frac{1-\nu^2}{E}\big)\big(\frac{p_0}{4a}\big)\int_0^{2\pi}a^2-r^2\cos^2 w\,dw \\ &= \big(\frac{1-\nu^2}{E}\big)\big(\frac{\pi p_0}{4a}\big)(2a^2-r^2). \end{aligned}$$

The quantity $u_S(r)$ is the displacement on only one of the surfaces, by defining a new constant E^*,

$$\frac{1}{E^*} := \frac{1-\nu_1^2}{E_1} + \frac{1-\nu_2^2}{E_2},$$

it is possible to express the total normal displacement by

$$u_{S_1}(r) + u_{S_2}(r) = \frac{\pi p_0}{4aE^*}(2a^2 - r^2) \tag{2.2}$$

for $0 < r \leq a$. Here, ν_1, ν_2 and E_1, E_2 denote Poisson's ratios and Young's modula for the two solids. However, since surface S_1 is rigid, $E_1 \to \infty$, $u_{S_1}(r) \equiv 0$, and

$$\frac{1}{E^*} = \frac{1 - \nu_2^2}{E_2}.$$

Alternatively, the normal displacement due to impact of a rigid sphere and a plane can be expressed by $u_{S_2}(r) = \delta - (R - \sqrt{R^2 - r^2})$ where δ is the maximum normal displacement and R is the radius of the sphere. Using $0 < r \leq a << R$,

$$u_{S_2}(r) = \delta - (R - \sqrt{R^2 - r^2}) = \delta - \frac{r^2}{R + \sqrt{R^2 - r^2}} \approx \delta - \frac{r^2}{2R}. \tag{2.3}$$

Setting equations (2.2) and (2.3) equal and equating coefficients yields the equations

$$\begin{aligned} \delta &= \frac{\pi p_0 a}{2E^*}, \\ \frac{1}{2R} &= \frac{\pi p_0}{4aE^*}. \end{aligned} \tag{2.4}$$

Solving both equations for E^*, equating the results, and solving for a produces the equation

$$a = \sqrt{R\delta}. \tag{2.5}$$

Solving equation (2.4) for p_0 results in the equation

$$p_0 = \frac{2aE^*}{\pi R}. \tag{2.6}$$

The total load P compressing the solids is related to the pressure by

$$P = \int_0^a \int_0^{2\pi} rp(r)\, d\theta\, dr = \frac{2\pi p_0}{a} \int_0^a r\sqrt{a^2 - r^2}\, dr = \frac{2}{3}\pi p_0 a^2. \tag{2.7}$$

Substituting equations (2.5) and (2.6) into equation (2.7) results in the Hertzian contact expression

$$P = \frac{4E^*\sqrt{R}}{3}\delta^{3/2}, \tag{2.8}$$

which relates the total load to the maximum displacement. It is precisely this term that will appear in our model of the impact oscillator.

2.2 The Melnikov Function

The Melnikov function is used in this thesis to determine continuation points of periodic solutions of the system

$$\dot{u} = f(u) + \epsilon g(u,t) \tag{2.9}$$

where $u \in \mathbb{R}^2$ and $g(u,t)$ a periodic function in t with period Ω. We also require the unperturbed system

$$\dot{u} = f(u) \tag{2.10}$$

to have a periodic orbit Γ with period Ω contained in a non-isochronous period annulus and that the period function is monotone in a neighborhood of Γ. Derivation of the Melnikov function also requires extensive use of Diliberto's Theorem, which is stated without proof.

Theorem 2.2.1 (Diliberto's Theorem)**.** *Let φ_t denote the flow of the differential equation $\dot{u} = f(u)$, $u \in \mathbb{R}^2$. If $f(\xi) \neq 0$, then the principal fundamental matrix solution $\Phi(t)$ at $t = 0$ of the homogeneous variational equation*

$$\dot{W} = Df(\varphi_t(\xi))W \tag{2.11}$$

with initial condition $W(0) = I$ *is such that*

$$\begin{aligned}\Phi(t)f(\xi) &= f(\varphi_t(\xi)),\\ \Phi(t)f^{\perp}(\xi) &= a(t,\xi)f(\varphi_t(\xi)) + b(t,\xi)f^{\perp}(\varphi_t(\xi))\end{aligned}$$

where

$$\begin{aligned}b(t,\xi) &= \frac{|f(\xi)|^2}{|f(\varphi_t(\xi))|^2} e^{\int_0^t \operatorname{div} f(\varphi_s(\xi))ds},\\ a(t,\xi) &= \int_0^t (2\kappa(s,\xi)|f(\varphi_s(\xi))| - \operatorname{curl} f(\varphi_s(\xi)))b(s,\xi)\, ds\end{aligned}$$

where $\kappa(t,\xi)$ *denotes the scalar curvature along* $\phi_t(\xi)$.

Let φ_t denote the flow of $\dot{u} = f(u)$ and ψ_t denote the flow of $\dot{u} = f^{\perp}(u)$. Then $\varphi_t(\xi) = u(t,\xi,0)$ where $u(t,\xi,\epsilon)$ is the solution to system (2.9) with initial condition ξ. We now define $R(\rho,\phi) := \varphi_\phi\psi_\rho(v)$ where $v \in \Gamma$ is arbitrary but fixed. The (ρ,ϕ) coordinates are defined in an annulus containing Γ and have the property that for ρ fixed, $R(\rho,\phi)$ is tangent to f and for $\phi \equiv 0$, $R(\rho,\phi)$ is tangent to $f^{\perp}$.

In these local coordinates, the displacement function in the Poincaré section with time slice Ω is given by

$$\Lambda(\rho,\phi,\epsilon) := \delta(R(\rho,\phi),\epsilon) \tag{2.12}$$

where $\delta(\xi,\epsilon) := u(\Omega,\xi,\epsilon) - \xi$ is the usual displacement function in the Poincaré section. The goal is to find implicit solutions of $\delta(\xi,\epsilon) = 0$ for small ϵ as these solutions correspond to continuation points.

Proposition 2.2.2. *Kernel* $\delta_\xi(\xi,0) = [f(\xi)]$ *where* $[v]$ *denotes the subspace spanned by the vector* v. *Moreover, the range of* $\delta_\xi(\xi,0)$ *is* $[f(\xi)]$.

Proof. Using the definition of the directional derivative and the group property of the unperturbed flow,

$$\begin{aligned}
\delta_\xi(\xi,0)f(\xi) &= \frac{d}{dt}\delta(u(t,\xi,0))|_{t=0} \\
&= \frac{d}{dt}(u(\Omega,u(t,\xi,0),0) - u(t,\xi,0))|_{t=0} \\
&= \frac{d}{dt}(u(\Omega+t,\xi,0) - u(t,\xi,0))|_{t=0} \\
&= f(u(\Omega,\xi,0)) - f(\xi) = 0.
\end{aligned}$$

This shows that $[f(\xi)] \subseteq \text{Kernel}\,\delta_\xi(\xi,0)$.

Consider the vector field $f^\perp$ and the solution $u^\perp(t,\xi)$ of the initial value problem $\dot{u} = f^\perp(u)$, $u(0) = \xi$. Then,

$$\begin{aligned}
\delta_\xi(\xi,0)f^\perp(\xi) &= \frac{d}{dt}(u(\Omega,u^\perp(t,\xi),0) - u^\perp(t,\xi))|_{t=0} \\
&= u_\xi(\Omega,\xi,0)f^\perp(\xi) - f^\perp(\xi)
\end{aligned}$$

where $u_\xi(t,\xi,0)$ is the principal fundamental matrix solution at $t = 0$ for the first variational equation

$$\begin{aligned}
\dot{W} &= Df(u(t,\xi,0))W, \qquad (2.13) \\
W(0) &= I.
\end{aligned}$$

Using Diliberto's theorem, $\delta_\xi(\xi,0)f^\perp(\xi) = a(\Omega,v)f(\xi) + (b(\Omega,v)-1)f^\perp(\xi)$. Since Γ is contained in a period annulus, $b(\Omega,v) = 1$ and

$$a(\Omega,v) = -\frac{|f(\xi)|^2}{\langle\dot{\sigma}(0), f^\perp(\xi)\rangle}T'(0) \neq 0$$

where $\dot{\sigma}(0)$ is the tangent vector to the Poincaré section at ξ determined by the parametrization and $\langle\cdot,\cdot\rangle$ is the usual inner product.

Using the above representations for a and b,

$$\delta_\xi(\xi,0)f^\perp(\xi) = a(\Omega,v)f(\xi) \neq 0. \tag{2.14}$$

Since $\operatorname{Kernel}\delta_\xi(\xi,0) \subseteq [f(\xi)]$ and $[f^\perp(\xi)] \not\subset \operatorname{Kernel}\delta_\xi(\xi,0)$, then $\operatorname{Kernel}\delta_\xi(\xi,0) = [f(\xi)]$ and as a consequence of equation (2.14), the range of $\delta_\xi(\xi,0) = [f(\xi)]$. □

We define $H(\rho,\phi,\epsilon) := P\cdot\Lambda(\rho,\phi,\epsilon)$ where $P := P(\phi)$ is the projection onto the range $[f(\varphi_\phi(v))]$ of the linear map $\delta_\xi(\varphi_\phi(v),0)$. Using the usual inner product, we can also define H by $(\rho,\phi,\epsilon) \mapsto \langle\Lambda(\rho,\phi,\epsilon), f(\varphi_\phi(v))\rangle$. So, $H_\rho(0,\phi,0)$ is given by $\langle\Lambda_\rho(0,\phi,0), f(\varphi_\phi(v))\rangle$.

Using Proposition 2.2.2 and Diliberto's theorem, we have

$$\begin{aligned}
\Lambda_\rho(0,\phi,0) &= \delta_\xi(\varphi_\phi(v),0)R_\rho(0,\phi)\\
&= \delta_\xi(\varphi_\phi(v),0)D\varphi_\phi(v)f^\perp(v)\\
&= \delta_\xi(\varphi_\phi(v),0)(a(\phi)f(\varphi_\phi(v)) + b(\phi)f^\perp(\varphi_\phi(v)))\\
&= b(\phi)\delta_\xi(\varphi_\phi(v),0)f^\perp(\varphi_\phi(v))\\
&= b(\phi)a(\Omega,v)f(\varphi_\phi(v)).
\end{aligned}$$

Thus,

$$H_p(0,\phi,0) = \langle b(\phi)a(\Omega,v)f(\varphi_\phi(v)), f(\varphi_\phi(v))\rangle = b(\phi)a(\Omega,v)|f(\varphi_\phi(v))|^2 \neq 0,$$

and we can apply the implicit function theorem to obtain an implicit function $\eta(\phi,\epsilon)$ such that $\eta(\phi,0) = 0$ and $H(\eta(\phi,\epsilon),\phi,\epsilon) \equiv 0$. Also, since the function produced by the implicit function theorem is unique and $\Lambda(0,\phi,0) \equiv 0$, then $\eta(\phi,0) \equiv 0$.

We want to consider the zeros of the reduced displacement function $\tilde{\Lambda}$ given by

$$(\phi,\epsilon) \mapsto Q(\phi)(\Lambda(\eta(\phi,\epsilon),\phi,\epsilon)) = \langle\Lambda(\eta(\phi,\epsilon),\phi,\epsilon), f^\perp(\varphi_\phi(v))\rangle$$

where $Q(\phi)$ is the linear projection onto the complement of the range of $\delta_\xi(\varphi_\phi(v), 0)$. We can also make the further reduction $\tilde{\Lambda}(\phi, \epsilon) = \epsilon(\tilde{\Lambda}_\epsilon(\phi, 0) + O(\epsilon))$ by expanding about $\epsilon = 0$.

Let us define the bifurcation function $B : \mathbb{R} \to \mathbb{R}$ by

$$B(\phi) := \tilde{\Lambda}_\epsilon(\phi, 0).$$

The simple zeros of B are the continuation points. In order to obtain an expression for the bifurcation function, compute the derivative of $\tilde{\Lambda}(\phi, \epsilon)$ at $\epsilon = 0$ to obtain the formula

$$B(\phi) = \langle \Lambda_\rho(0, \phi, 0)\eta_\epsilon(\phi, 0) + \Lambda_\epsilon(0, \phi, 0), f^\perp(\varphi_\phi(v))\rangle = \langle \Lambda_\epsilon(0, \phi, 0), f^\perp(\varphi_\phi(v))\rangle. \quad (2.15)$$

To find a formula for the partial derivative $\Lambda_\epsilon(0, \phi, 0)$, use the definition $\delta(\xi, \epsilon) = u(\Omega, \xi, \epsilon) = \xi$ to obtain the equation

$$\Lambda_\epsilon(0, \phi, 0) = u_\epsilon(\Omega, \varphi_\phi(v), 0). \quad (2.16)$$

The linear map $u_\epsilon(\Omega, \xi, 0)$ is the solution of the second variational equation $\dot{W} = Df(\varphi_t(\xi))W + g(\varphi_t(\xi))$, $W(0) = 0$. The solution is given by the variation of constants formula

$$u_\epsilon(\Omega, \xi, 0) = \Phi(\Omega) \int_0^\Omega \Phi^{-1}(s) g(\varphi_s(\xi)) ds \quad (2.17)$$

where $\Phi(t)$ is the principal fundamental matrix solution of the first variational equation (2.13) which is represented as a linear transformation by

$$\Phi(t) = \begin{pmatrix} 1 & a(t, \xi) \\ 0 & b(t, \xi) \end{pmatrix}.$$

In order to simplify the formula given by variation of constants, let us express g in the form $g(\varphi_t(\xi),t) = c_1(t,\xi)f(\varphi_t(\xi)) + c_2(t,\xi)f^{\perp}(\varphi_t(\xi))$ where

$$\begin{aligned} c_1(t,\xi) &= \frac{1}{|f(\varphi_t(\xi))|^2}\langle g(\varphi_t(\xi),t), f(\varphi_t(\xi))\rangle, \\ c_2(t,\xi) &= \frac{1}{|f(\varphi_t(\xi))|^2} f(\varphi_t(\xi) \wedge g((\varphi_t(\xi),t). \end{aligned}$$

Substituting the expressions for Φ and g into equation (2.17) and simplifying yields the equation

$$u_\epsilon(\Omega,\xi,0) = (\bar{N}(\xi) + a(\Omega,\xi)\bar{M}(\xi))f(\xi) + \bar{M}(\xi)f^{\perp}(\xi) \tag{2.18}$$

where M and N are defined by

$$\begin{aligned} \bar{M}(\xi) &:= \frac{1}{|f(\xi)|^2}\int_0^{\Omega} e^{-\int_0^s \operatorname{div} f(\varphi_t(\xi))dt} f(\varphi_s(\xi)) \wedge g(\varphi_s(\xi))\, ds, \\ \bar{N}(\xi) &:= \int_0^{\Omega} \frac{1}{|f(\varphi_s(\xi))|^2}\langle g(\varphi_s(\xi)), f(\varphi_s(\xi))\rangle\, ds \\ &\quad - \int_0^{\Omega} \frac{a(s,\xi)}{b(s,\xi)|f(\varphi_s(\xi))|^2} f(\varphi_s(\xi)) \wedge g(\varphi_s(\xi))\, ds. \end{aligned}$$

Replacing ξ by $\varphi_\phi(v)$ and substituting equation (2.18) into equation (2.15) yields the the simplified representation

$$B(\phi) = |f(\varphi_\phi(v))|^2 \bar{M}(\phi).$$

Thus, ϕ is a continuation point if and only if ϕ is a simple zero of the Melnikov function

$$M(\phi) := \int_0^{\Omega} e^{-\int_0^s \operatorname{div} f(\varphi_{t+\phi}(v))dt} f(\varphi_{s+\phi}(v)) \wedge g(\varphi_{s+\phi}(v),t).$$

The sign of the Melnikov function determines the drift in a direction transverse to the unperturbed orbit Γ. Also, since the period function is monotone in a neighborhood of Γ, the drift of the unperturbed Poincaré map is in opposite directions

on opposite sides of the resonant orbit. A plot of these directions at two continuation points is shown in Fig. 2.2. The configuration shown in Fig. 2.3 is called an island chain. For a more in-depth study of invariant chaotic sets and transient chaotic behavior present in the island chain configuration see [3].

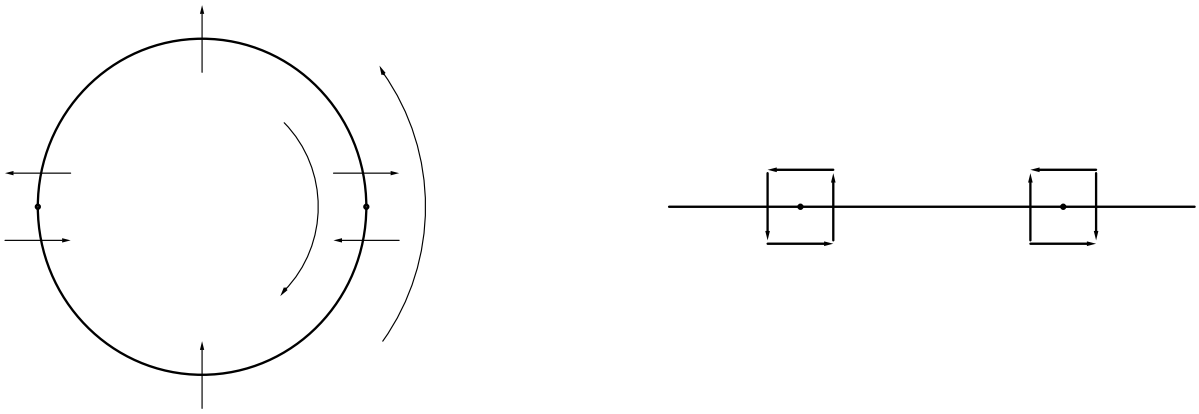

Figure 2.2: The left figure depicts a resonant periodic orbit as a manifold of fixed points in the Poincaré section. In this illustration, the two larger points represent the continuation points corresponding to the zeros of the Melnikov function. The "twist" in the tangential directions is due to the changing period function while the normal "push" directions are due to the perturbation as detected by the Melnikov function. The right figure shows the local directions of twist and push near these continuation points.

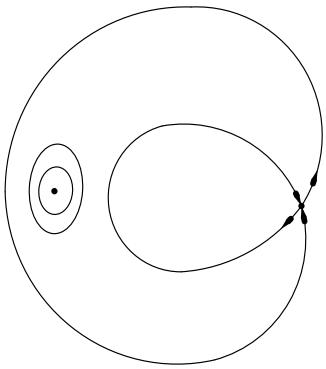

Figure 2.3: This figure depicts the continuation points in Fig. 2.2 after perturbation. The stability types are as would be expected given the twist and push near those points. The rotation point is depicted as a center in this illustration, but it can be a source or a sink depending on the nature of the perturbation.

Chapter 3

The Impact Oscillator

3.1 Introduction

The behavior of piecewise smooth dynamical systems has practical relevance to many areas of science and engineering. For instance, motion dependent discontinuities are often deliberately included in machinery models to accommodate part tolerances, a working clearance, or the finite accuracy of a manufacturing process [19]. Other examples include gear trains with backlash, systems with dry friction, and the application of impact dampers for vibration amplitude reduction. Much of the previous work on systems modeling the impact of two solids has focused on piecewise linear systems that have a discontinuity in the force-displacement relationship. Although these systems are piecewise linear, the mere presence of a discontinuity—in these otherwise linear systems—allows for the manifestation of highly nonlinear behavior [25]. While impact oscillators have been studied extensively (see [1, 2, 11, 12, 15, 19, 17, 18, 20, 21, 22, 24, 25, 26, 28]), the full range of associated phenomena remains to be explored.

We will investigate the predictions of a mathematical model for a laboratory apparatus consisting of a pendulum and an elastic barrier, which are rigidly attached to

a shaker table, together with computerized data acquisition for the pendulum's angular position. Our model incorporates Hertzian contact between the spherical steel pendulum bob and the aluminum alloy barrier.

We show that our model captures the qualitative and quantitative behavior of the impact oscillator; and, we report a new qualitative effect: In the impact regime for a predictable range of energies, the oscillation frequency increases for small increases in energy near grazing, reaches a maximum and then *decreases* for moderate increases in impact energies, and increases again as the energy is further increased. This phenomenon is explained in detail and demonstrated using experimental data. In addition, we discuss experimental verification of a theoretical prediction, involving synchronization of the system with periodic external forcing at resonance, that follows from the existence of this non-monotonicity.

3.2 Mathematical Model

Consider a horizontally periodically forced pendulum that encounters a barrier when the pendulum's angular position x (measured counterclockwise relative to the downward vertical) is x_c (see Fig. 3.1).

The kinetic energy for the pendulum, forced at an excitation frequency Ω and amplitude A, is

$$T = \frac{1}{2}m\Big[\Big(A\Omega\cos\Omega t + L\dot{x}\cos x\Big)^2 + \Big(L\dot{x}\sin x\Big)^2\Big],$$

where m is the pendulum mass and L is the pendulum effective length. Here, the pendulum effective length refers to the distance between the pendulum pivot point and the pendulum center of mass. Because the mass in this physical system is distributed

along the pendulum shaft and bob, the effective length differs from the total length, l, which is the distance from the pivot to the sphere center of mass. The pendulum's potential energy when not in contact with the barrier is

$$V = mgL(1 - \cos x).$$

Using Lagrange's equation

$$\frac{d}{dt}\Big(\frac{\partial T}{\partial \dot{x}}\Big) - \frac{\partial T}{\partial x} + \frac{\partial V}{\partial x} = 0$$

and inserting damping forces, the equation of motion for the pendulum during the contact and non-contact regimes is

$$\ddot{x} + 2\zeta\omega\dot{x} + \alpha\omega^2 \operatorname{sgn}(\dot{x}) - \frac{A\Omega^2}{L}\sin\Omega t\cos x + \omega^2 \sin x + \frac{l}{mL^2}H(x - x_c)(F_c(x - x_c) + V_c(\dot{x}, x - x_c)) = 0, \tag{3.1}$$

where H is the Heaviside function, F_c is the contact force function that occurs at distance l from the pendulum pivot point, V_c is the elastic damping force, ζ is the viscous damping ratio, $\omega^2 = g/L$ is the square of the pendulum's natural frequency, $\alpha\omega^2$ is the magnitude of the Coulomb damping, and H is the Heaviside function.

The Hertzian contact force is given by

$$F_c(x) = \frac{4}{3}E\sqrt{R}(l\sin x)^{3/2},$$

where E is the elastic modulus of the aluminum alloy (AL 7050-T7651) barrier and R is the radius of the sphere that impacts the barrier. We take the elastic damping force to be

$$V_c(\dot{x}, x) = \mu\omega\dot{x}(\sin x)^{3/2}, \tag{3.2}$$

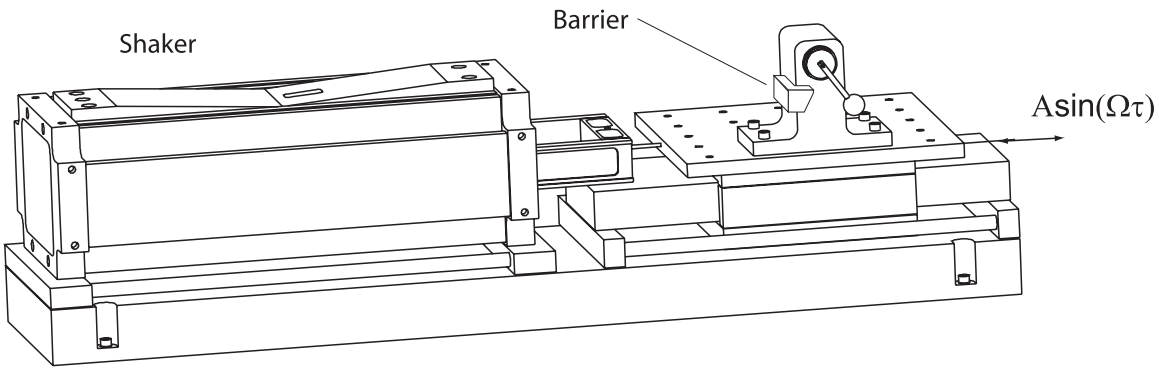

Figure 3.1: Schematic drawing of the experimental apparatus. The pendulum pivot and the barrier are rigidly attached to a shaker table that is designed to oscillate horizontally at a specified amplitude and frequency.

where μ is the barrier damping coefficient (see [12, 19]).

The equation of motion (3.1) is made non-dimensional by changing the time-scale via $t \mapsto t/\omega$. After simplifying and replacing the sine function in the contact term by the first term of its Taylor series centered at x_c (which is justified by the small penetration depth and the presence of the Heaviside function factor), and replacing the Coulomb damping term $\operatorname{sgn}(\dot{x})$ by the smooth approximation $2/\pi \arctan(100\dot{x})$, we obtain the smooth dimensionless model equation

$$\ddot{x} + 2\zeta\dot{x} + \alpha\frac{2}{\pi}\arctan(100\dot{x}) \\ -\beta\sin(\frac{\Omega}{\omega}t)\cos x + \sin x + (\gamma + \mu\dot{x})(x - x_c)^{3/2}H(x - x_c) = 0, \tag{3.3}$$

where

$$\beta = \frac{A\Omega^2}{\omega^2 L}, \qquad \gamma = \frac{4l^{5/2}ER^{1/2}}{3\omega^2 mL^2}.$$

While the equation of motion incorporates the discontinuous Heaviside function, we note that the contact term is class C^1 due to the presence of the Hertzian penetration function given in the model equation (3.3) by $(x - x_c)^{3/2}$.

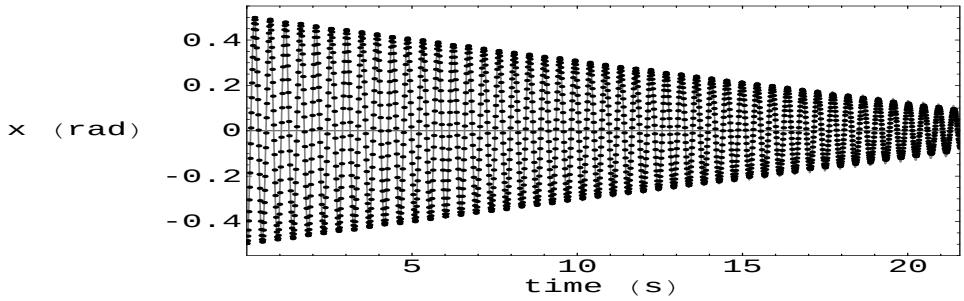

Figure 3.2: Overlay of graphs of the angular position versus time of the unforced pendulum with no barrier obtained by simulation and experiment using the pendulum estimated parameters given in display (3.4). Time series show experimental data (represented by dots) and the simulated data (continuous line).

The physical parameters corresponding to our apparatus are

$$\begin{gathered} m \approx 0.0326\,\mathrm{Kg}, \quad R \approx 0.0095\,\mathrm{m}, \quad l \approx 0.0524\,\mathrm{m}, \quad x_c \approx 0.323, \\ \omega \approx 13.752\,\mathrm{sec}^{-1}, \quad L = \frac{g}{\omega^2} \approx 0.0519\,\mathrm{m}, \quad \zeta \approx 0.000145, \quad \alpha \approx 0.00206. \end{gathered} \tag{3.4}$$

The (dimensionless) damping ratios ζ and α along with the pendulum's natural frequency ω are identified from experimental data, for the unforced pendulum with no barrier, by a least squares minimization procedure. The barrier damping coefficient μ and the dimensionless parameter γ, which is proportional to the elastic modulus E, are determined similarly from experimental data for the unforced pendulum with barrier. The amplitude A and frequency Ω are control parameters.

The statically measured parameter values for m, R, and l together with the identified values of ζ, α and ω give a good fit to experimental data for the unforced pendulum with no barrier (see Fig. 3.2).

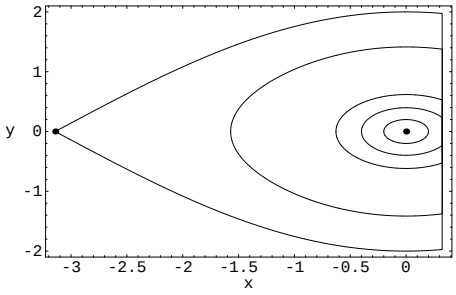

Figure 3.3: Phase portrait for the undamped, unforced impact oscillator, where x is the angular position and y is the velocity.

3.3 The Undamped Unforced Pendulum With Barrier

We set $\zeta = \alpha = \mu = \beta = 0$ in equation (3.3) and consider the equivalent first-order system

$$\begin{pmatrix} \dot{x} \\ \dot{y} \end{pmatrix} = \begin{pmatrix} y \\ -\sin x - \gamma(x - x_c)^{\frac{3}{2}} H(x - x_c) \end{pmatrix} = f(x, y). \tag{3.5}$$

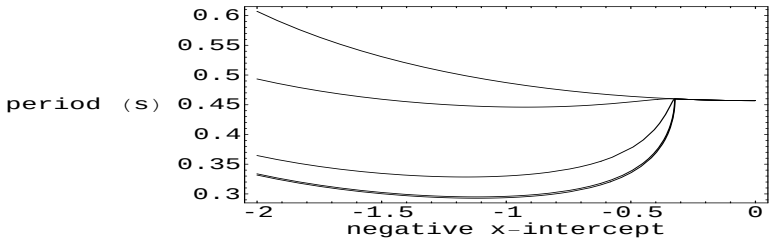

Figure 3.4: The figure shows the graphs of period functions of system (3.5), where the horizontal axis is the negative x-intercept of the periodic orbits. We associate each periodic orbit with its negative x-intercept. The graphs are for the undamped unforced system (3.5) converted to the original time measured in seconds (i.e. the periods are divided by ω). The corresponding graphs appear in the order $\gamma = 0, 1, 10^2, 10^5, 10^9$ in the figure from top to bottom.

Linearizations at the physically realistic rest points of system (3.5), $(0, 0)$ and

$(-\pi, 0)$, correspond to the (linear) system matrices

$$Df(0,0) = \begin{pmatrix} 0 & 1 \\ -1 & 0 \end{pmatrix}, \qquad Df(-\pi, 0) = \begin{pmatrix} 0 & 1 \\ 1 & 0 \end{pmatrix}.$$

By the usual analysis, using their eigenvalues and eigenvectors, it follows that $(-\pi, 0)$ is a hyperbolic saddle point with stable manifold tangent to $y = -x$ and unstable manifold tangent to $y = x$. The rest point $(0, 0)$ is non-hyperbolic; it corresponds to a linear center. System (3.5) is Hamiltonian, with Hamiltonian

$$E(x, y) = \frac{1}{2}y^2 - \cos x + \frac{2}{5}\gamma(x - x_c)^{\frac{5}{2}}H(x - x_c) + 1.$$

Since orbits of system (3.5) lie on level sets of E, it follows that $(0, 0)$ is a center. The phase portrait of system (3.5) is depicted in Fig. 3.3. The region of the phase portrait corresponding to the physical regime is a homoclinic loop at the saddle point surrounding an annulus of periodic orbits whose inner boundary is the center at the origin. Because the depth of the penetration of the pendulum mass into the barrier is very small compared with the scale of the figure, the periodic orbits surrounding the center and the homoclinic orbit depicted in the figure appear to merge into a vertical line segment at the angular value $x_c = 0.323$. Of course, these orbits do not intersect.

A numerical approximation of the graph of the period function, which is defined on the interval $(-\pi, 0)$ in the negative x-axis by assigning to each point in this interval the minimum period of the corresponding periodic orbit with this intercept, is depicted in Fig. 3.4. The period annulus consisting of all such periodic orbits with intercept in this interval is bounded by the homoclinic loop of system (3.5). The negative direction of the horizontal axis corresponds to an increase in energy. Note the shape of the graph, as described in Section 3.1: The period function is not monotonic as

it would be for the pendulum with no barrier; instead, the period function has two critical points. The critical point near -0.3 (a relative maximum) corresponds to the effect of the barrier. But, of course, due to the smoothness of the graph, this critical point does not occur exactly at the orbit corresponding to grazing the barrier. Rather, it occurs at an orbit with slightly larger energy, which corresponds to a positive penetration depth at the barrier. Fig. 3.4 shows the period function (with respect to the time measured in seconds) for several values of the parameter γ. The graph for $\gamma = 0$ depicts the graphs of the period function for the pendulum in case no barrier is present. In this case, as is well-known, the period function increases as energy increases.

By inspection of Fig. 3.4, it appears that the periods decrease as γ increases. The minimum period for $\gamma = 10^9$ (which corresponds to the elasticity coefficient $E \approx 2.03 \times 10^{11}$) is approximately 0.3 sec. The corresponding frequency is approximately 3.33 Hz. We also note that the local maximum period corresponding to the critical point near 0.3 is approximately 0.46 sec, which corresponds to the approximate frequency of 2.17 Hz. While resonance is theoretically possible outside this interval, for example, in the range of energies higher than the energy of the orbit corresponding to the minimum of the period function, our experiments are restricted to the range of smaller energies. We will show that the theoretical range of values is consistent with physical experiments. A proof of the non-monotonicity of the period function for the model equation (3.5), for the case of large γ and barrier position at the downward vertical, is given in the next chapter.

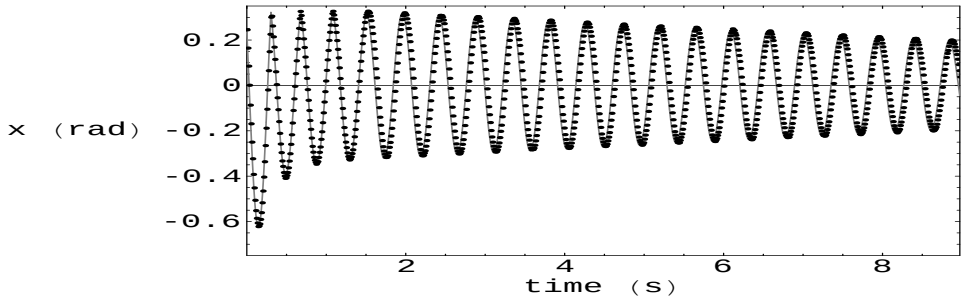

Figure 3.5: Overlay of angle versus time for the unforced, damped pendulum with barrier for experimental data (dotted) and simulation (continuous). Here, we have used $\gamma = 2.71 \times 10^9$(corresponding to elastic modulus $E = 5.5 \times 10^{11}\,\mathrm{N/m^2}$) and barrier damping coefficient $\mu = 9.69 \times 10^9$.

3.4 The Damped Unforced Pendulum With Barrier

With $\beta = 0$, $\zeta > 0$, $\alpha > 0$, and $\mu > 0$ in equation (3.3), the equivalent first-order system is

$$\begin{aligned} \dot{x} &= y, \\ \dot{y} &= -2\zeta y - \alpha\frac{2}{\pi}\arctan(100y) - \sin x \\ &\quad - (\gamma + \mu y)(x - x_c)^{\frac{3}{2}} H(x - x_c). \end{aligned} \tag{3.6}$$

The physically realistic rest points of system (3.6) are $(-\pi, 0)$ and $(0, 0)$. Linearizations at the rest points yield the matrices

$$Df(0,0) = \begin{pmatrix} 0 & 1 \\ -1 & -2\zeta - \frac{200\alpha}{\pi} \end{pmatrix}, \qquad Df(-\pi,0) = \begin{pmatrix} 0 & 1 \\ 1 & -2\zeta - \frac{200\alpha}{\pi} \end{pmatrix}.$$

An eigenvalue analysis shows that $(0, 0)$ is a hyperbolic sink and $(-\pi, 0)$ is a hyperbolic saddle with stable and unstable manifolds in the same orientation as in system (3.5).

The barrier damping coefficient μ and the elastic modulus γ are identified from experimental data obtained by releasing the pendulum from rest at several different

heights exceeding the height of the barrier. While the supposed form (3.2) of the elastic damping is of course a phenomenological choice, this functional form is consistent with experiment. For example, Fig. 3.5 shows the graphs for corresponding experimental data and simulation for the pendulum released from rest at approximately -0.73 radians from the downward vertical in the direction opposite to the position of the barrier at $x_c = 0.323$ radians. By numerical integration we find favorable fitting for γ in the range 10^8–10^{11}. This is consistent with the expected elastic coefficient $E = 7.11 \times 10^{10}$ ($\gamma = 3.5 \times 10^8$) of the aluminum barrier AL 7050-T7651. The values that produce the smallest least squares error are $\gamma = 2.71 \times 10^9$ and $\mu = 9.69 \times 10^9$. This γ value corresponds to elastic modulus $E = 5.5 \times 10^{11}$.

3.5 The Forced Damped Pendulum With Barrier

For $\beta > 0$, the system described in equation (3.3) is not autonomous. The corresponding first-order system is

$$\begin{aligned} \dot{x} &= y, \\ \dot{y} &= -2\zeta y - \alpha\frac{2}{\pi}\arctan(100y) - \sin x \\ &\quad - (\gamma + \mu y)(x - x_c)^{\frac{3}{2}} H(x - x_c) + \beta \sin(\frac{\Omega}{\omega}\, t)\cos x, \end{aligned} \tag{3.7}$$

or, in a more compact form

$$\begin{pmatrix} \dot{x} \\ \dot{y} \end{pmatrix} = f(x, y) + \begin{pmatrix} 0 \\ \beta \sin(\frac{\Omega}{\omega}\, t)\cos x \end{pmatrix}.$$

We expect frequency locking (for small damping and small amplitude forcing) at $(1:1)$-resonance; that is, in case the forcing (circular) frequency Ω/ω is equal

Hz	$\Omega/(2\pi)$	x_f
0.75	0.70	2.30
1.25	1.24	1.24
1.50	1.48	3.00
1.75	1.76	1.76
2.00	2.00	2.00
2.25	2.24	2.24
2.50	2.52	2.52
2.75	2.76	2.76
3.00	3.00	3.00
3.25	3.24	3.24
3.50	3.52	3.52
3.60	3.60	3.60
3.75	3.76	3.76
4.00	4.00	4.00
4.25	4.24	4.24
4.50	4.52	2.24

Table 3.1: Experimental data recorded with the shaker table frequencies set to the values in the left-hand column. The corresponding values in the second and third columns are the computed frequencies (of the shaker table and the angular response of the pendulum motion) from a Fourier analysis of the data. They correspond to the highest peaks in the respective spectral amplitudes. Note that the motion is locked in $(1:1)$-resonance with the parametric periodic force for the input range 1.75–4.25 Hz. The motion is not in $(1:1)$-resonance for input frequencies 0.75, 1.50 and 4.50 Hz.

to a natural frequency of the unforced undamped pendulum with barrier (see, for example, [3, 10, 27]). The available natural frequencies are determined by the period function described in Section 3.3.

Recall from our discussion in Section 3.3 that the period function *decreases* as energy increases in an interval near (but not containing) the position of the barrier. Thus, $(1:1)$-resonances will occur for periodic parametric forcing with frequencies much higher than for the corresponding pendulum with no barrier, which has an increasing period function. From the bottom graph in Figure 3.4, the approximate range of available natural frequencies (corresponding to the energy range explored in our experiments) is 2.17–3.33 Hz. According to the experimental data given in Table 3.1, the physical forced pendulum is locked in $(1:1)$-resonance over the forcing frequency range 1.75–4.25 Hz. The theoretical region predicted by the model assumes small damping and small amplitude forcing; and, of course, the experimental data has some error due to measurement. While the theoretical range is not expected to match the experimental range exactly, the qualitative behavior predicted by the theory is verified by our experiments. The frequency spectra for some of the experimental data corresponding to Table 3.1 are depicted in Figures 3.6, 3.7, and 3.8. Figure 3.6 shows an example of $(1:1)$ resonance locking, Figure 3.7 shows an example not locked in $(1:1)$ resonance, and Figure 3.8 shows the change in frequency spectra of the response as the forcing frequency moves through the region of $(1:1)$ resonance locking. Our theoretical prediction of the range of $(1:1)$ resonance locking is verified by the experimental data.

The lower bound of the frequency locking range is less than that expected for

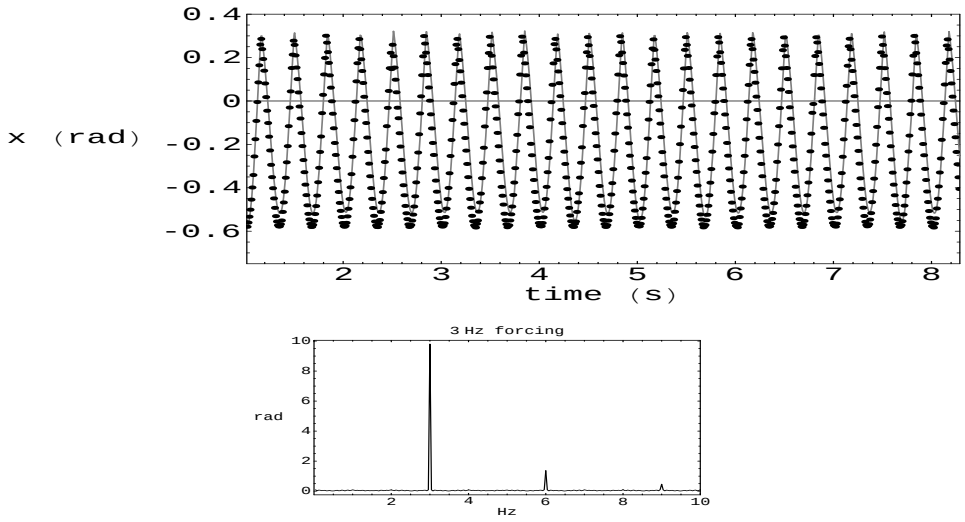

Figure 3.6: The top panel shows an overlay of angle versus time for the forced damped pendulum with barrier for experimental data (dotted) and simulation (continuous) for $\gamma = 2.71 \times 10^9$ (corresponding to elastic modulus $E = 5.5 \times 10^{11}\,\mathrm{N/m^2}$) and barrier damping coefficient $\mu = 9.69 \times 10^9$. The shaker table is forced with amplitude 0.0027 m and frequency 3 Hz. The bottom panel is the frequency spectrum of the experimental data. The peak at 3 Hz corresponds to the $(1:1)$ resonance.

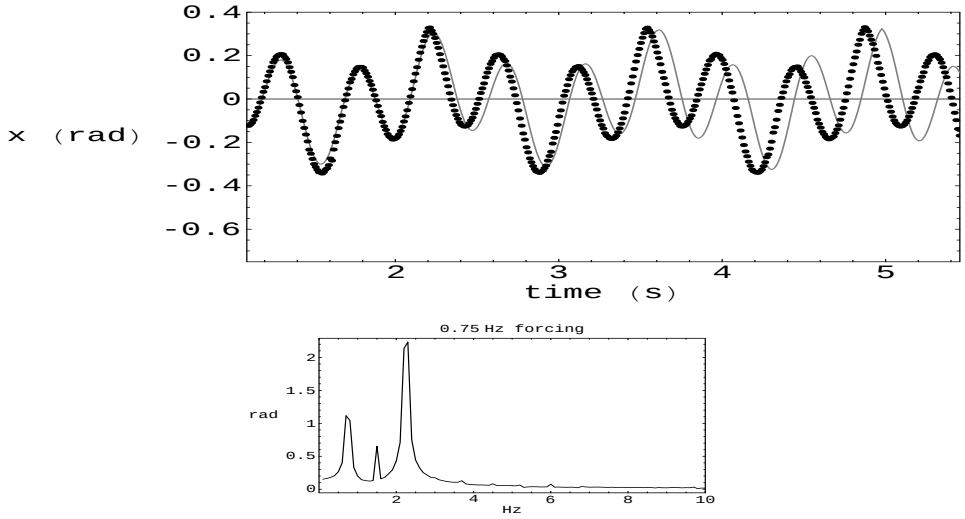

Figure 3.7: The top panel shows an overlay of angle versus time (in seconds) for the forced damped pendulum with barrier for experimental data (dotted) and simulation (continuous) for $\gamma = 2.71 \times 10^9$ (corresponding to elastic modulus $E = 5.5 \times 10^{11}\,\mathrm{N/m^2}$) and barrier damping coefficient $\mu = 9.69 \times 10^9$. The shaker table is forced with amplitude 0.0401 m and frequency 0.75 Hz. The bottom panel is the frequency spectrum of the experimental data. There is no dominant peak corresponding to $(1:1)$ resonant with the forcing; the oscillator is not locked in $(1:1)$ resonance.

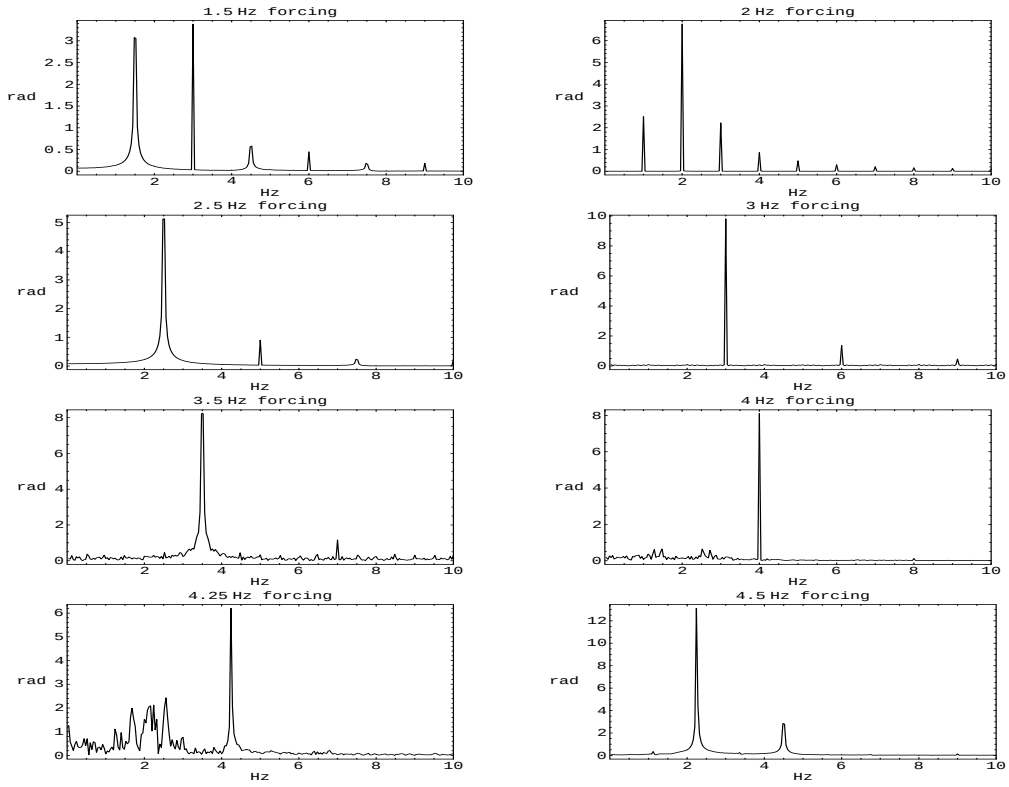

Figure 3.8: Frequency spectra of experimental data for a range of forcing frequencies. There is no dominant peak corresponding to $(1:1)$ resonance for 1.50 Hz or 4.50 Hz forcing, but dominant $(1:1)$ resonant peaks exist for all frequencies between 2.00 Hz and 4.25 Hz.

the pendulum with no barrier. This is a consequence of our basic discovery: the response period of the unforced undamped pendulum reaches a local maximum at some critical amplitude larger than the amplitude of the pendulum corresponding to the barrier position. The period *decreases* as the amplitude is increased beyond this critical value until the amplitude reaches a second critical value at which the response period is a minimum. For amplitudes that exceed this second critical value, the period increases with increasing amplitude. The available periods of unforced periodic orbits is increased from the interval of available periods for the pendulum with no barrier to include the interval of periods bounded by the first and second critical values.

3.6 Existence of Harmonics

In the previous sections, we showed the existence of a non-monotone period function for the unforced and undamped pendulum with barrier and $(1:1)$ resonance for forced oscillations near the contact regime. In this section, using Melnikov theory, we will prove the existence of harmonics. To apply this theory, the forcing and damping terms must be small. We satisfy this requirement in our model equation by incorporating these terms as a first-order perturbation, with respect to a new (dimensionless) parameter ϵ, of the unforced and undamped pendulum with barrier model. We will prove the existence of harmonics for sufficiently small ϵ. While we do not prove the existence of harmonics for the true model equations ($\epsilon = 1$), the main point here is that perturbed periodic solutions do exist for our mathematical model near resonances in the regime with damping and forcing. This provides evidence that our computer experiments, which show the existence of harmonics for the model equation

with physically correct parameters, are valid and this agrees with the experimental evidence of frequency locking.

Let us examine the system

$$\begin{aligned}
\dot{x} &= y \\
\dot{y} &= -\sin x - \gamma(x - x_c)^{\frac{3}{2}} H(x - x_c) \\
&\quad + \epsilon(-2\zeta y - \alpha \frac{2}{\pi} \arctan(100y) + \beta \sin(\frac{\Omega}{\omega} t) \cos x \\
&\quad - \mu y (x - x_c)^{\frac{3}{2}} H(x - x_c)),
\end{aligned} \tag{3.8}$$

or, more compactly,

$$\begin{pmatrix} \dot{x} \\ \dot{y} \end{pmatrix} = f(x, y) + \epsilon g(x, y, t, \epsilon).$$

Using numerical approximation of solutions of the unperturbed ($\epsilon = 0$) system, we will show the existence (for small ϵ) of an attractor—a stable periodic orbit—corresponding to a stable periodic point in a (stroboscopic) Poincaré section. In view of the damping in our system, it is well-known that it suffices to demonstrate that the Melnikov function, given by

$$M(l) = \int_{-T}^{T} f(x(\sigma), y(\sigma)) \wedge g(x(\sigma), y(\sigma), \sigma + l, 0) \, \mathrm{d}\sigma,$$

where $t \mapsto (x(t), y(t))$ is an unperturbed solution on a resonant unperturbed periodic orbit with period $2T$, has simple zeros and the derivative of the corresponding period function does not vanish at the resonant orbit (see, for example, [3, 10, 27] for background on the Melnikov function) and $\wedge$[1] is the wedge product.

By substitution using equation (3.8) and some simplification, the Melnikov func-

[1] $(a, b) \wedge (c, d) := ad - bc$

tion is recast in the form

$$M(l) = \zeta I_1 + \alpha I_2 + \mu I_3 + \beta \cos(\frac{\Omega}{\omega} l) I_4 + \beta \sin(\frac{\Omega}{\omega} l) I_5,$$

where I_1,I_2, I_3, I_4 and I_5 are given by

$$\begin{aligned}
I_1 &= \int_{-T}^{T} -2y^2(\sigma)\ \mathrm{d}\sigma, \\
I_2 &= \int_{-T}^{T} -\tfrac{2y}{\pi}(\sigma) \arctan(100y(\sigma))\, \mathrm{d}\sigma, \\
I_3 &= \int_{-T}^{T} -y^2(\sigma)(x(\sigma) - x_c)^{3/2} H(x(\sigma) - x_c)\, \mathrm{d}\sigma, \\
I_4 &= \int_{-T}^{T} y(\sigma) \cos(x(\sigma)) \sin(\tfrac{\Omega}{\omega}\sigma)\ \mathrm{d}\sigma, \\
I_5 &= \int_{-T}^{T} y(\sigma) \cos(x(\sigma)) \cos(\tfrac{\Omega}{\omega}\sigma)\ \mathrm{d}\sigma,
\end{aligned}$$

$x(0)$ is the positive x-intercept and $2T$ is the period.

The first four integrals can only be calculated numerically, but the integrand of I_5 is an odd function in σ, so $I_5 = 0$. This reduces the Melnikov function to

$$M(l) = \zeta I_1 + \alpha I_2 + \mu I_3 + \beta \cos(\frac{\Omega}{\omega} l) I_4. \tag{3.9}$$

If $I_4 \neq 0$ and the inequality

$$\left| \frac{\zeta I_1 + \alpha I_2 + \mu I_3}{\beta I_4} \right| < 1 \tag{3.10}$$

is satisfied, then M has simple zeros; that is, there exists l_0 such that $M(l_0) = 0$ and $M'(l_0) \neq 0$. For example, in case the unperturbed orbit has period $2\pi\Omega/\omega$ ($(1:1)$-resonance), there are exactly two simple zeros.

The dimensionless forcing is $2\pi\omega/\Omega$ periodic, so we must compute the Melnikov function on unperturbed (resonant) orbits of system (3.8) (with $\epsilon = 0$) whose periods are rational multiples of $2\pi\omega/\Omega$. The physical regime for our experiments consists of orbits close to the rest point at $(0, 0)$. For each choice of the parameters, we consider

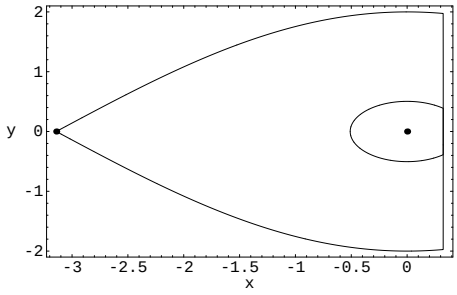

Figure 3.9: Plot of the homoclinic loop and a $(1:1)$-resonant orbit for the identified parameter values $\gamma = 2.71 \times 10^9$ and $\mu = 9.69 \times 10^9$.

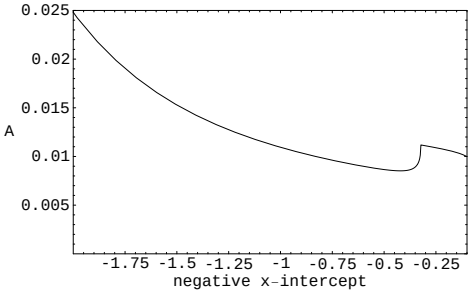

Figure 3.10: Plot of x-intercept vs amplitude of forcing in centimeters for the identified parameter values $\gamma = 2.71 \times 10^9$ and $\mu = 9.69 \times 10^9$. The region above the curve is where inequality (3.10) is satisfied; that is, simple zeros of the Melnikov function exist.

an orbit close to this rest point whose period is $(1:1)$-resonant with the shaker period. For example, suppose the dimensional forcing frequency is 3 Hz ($\Omega = 6\pi\,\mathrm{sec}^{-1}$). Using $E = 5.5 \times 10^{11}$ ($\gamma = 2.71 \times 10^9$) and $\mu = 9.69 \times 10^9$, the $(1:1)$-resonant orbit closest to $(0,0)$ has negative x-intercept $x \approx -0.51$ (see Fig. 3.9 for a plot of the resonant orbit). Also, from our numerical calculations, the derivative of the period function is positive at this orbit.

Inequality (3.10) is an equality whenever the dimensional amplitude of forcing is given by

$$A = \frac{\omega^2 L}{\Omega^2} \left| \frac{\zeta I_1 + \alpha I_2 + \mu I_3}{I_4} \right|.$$

A plot of A versus the negative x-intercept of the unperturbed periodic orbit is de-

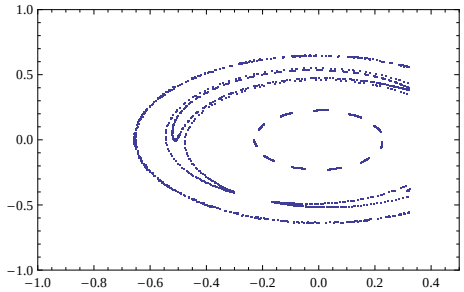

Figure 3.11: Four orbits of the Poincaré map in the Poincaré section for system (3.8) at the time slice $2\pi\omega/\Omega$ with $\Omega = 6\pi$, $\epsilon = 0.001$, and $A = 0.03$m, but with no damping (i.e. with ζ, α, and μ set to zero). The initial points are (x, y) equal to $(-0.65, 0.0)$, $(-0.544, 0.0)$, $(-0.510, 0.0)$, and $(-0.23, 00)$. The orbit corresponding to $(-0.65, 0.0)$ appears to correspond to an invariant torus with a dense orbit, the orbits corresponding to $(-0.544, 0.0)$ and $(-0.510, 0.0)$ are in the island surrounding the stable harmonic at $(1 : 1)$ resonance with the sharp points of the outer orbit indicating the presence of a harmonic of saddle type, and the orbit corresponding to $(-0.23, 0.0)$ (which is in the libration regime that does not contact the barrier) is near a high-order resonance.

picted in Fig. 3.10. The region above the curve corresponds to the intercepts and forcing amplitudes that satisfy inequality (3.10).

As long as $A > 0.0087$ cm, the necessary inequality is satisfied and $M(l)$ has a simple zero. So, for sufficiently small ϵ, the set of resonant periodic orbits will break into the familiar "island chain" configuration [3]. Fig. 3.11 depicts a typical example for the case of no damping, where the $(1, 1)$ resonance is dominant but other high-order resonances also produce island chains at a smaller scale (of island width). In the presense of damping, the sizes of the basins of attraction of stable harmonics can be very small, but we expect the attractor near the $(1 : 1)$-resonance to be dominant. In our numerical experiments, phase locking occurs for the entire frequency range given in Section 3.5. A plot of a simulated orbit in a Poincaré section for system (3.8) is shown in Fig. 3.12. The orbit appears to converge to a stable fixed point of the Poincaré map, which corresponds to an asymptotically stable harmonic of

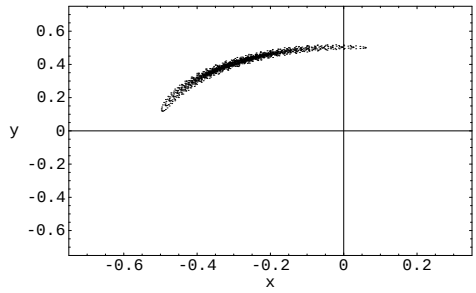

Figure 3.12: An orbit of the Poincaré map in the Poincaré section for system (3.8) at the time slice $2\pi\omega/\Omega$ with $\Omega = 6\pi$, $\epsilon = 0.001$ and $A = 0.03$m. The initial point is in the third quadrant near a zero of the Melnikov function for the $(1:1)$-resonant orbit. The solution is numerically integrated over the time interval $[0, 2\pi\omega/\Omega]$ and the final value is saved; it is the value of the Poincaré map applied to the initial point. The time is reset to zero, and the system is integrated again over the same interval using the final point as the new initial value. This process (the Poincaré return map) is iterated 500 times after which the next 1500 final points are plotted. This simulated orbit of the Poincaré map appears to converge to a stable fixed point.

the forced oscillator. This asymptotically stable harmonic is near the stable harmonic in Fig. 3.11.

3.7 Conclusion

We have demonstrated that the Hertzian contact model fits data very well for the impact pendulum and also proven the existence of harmonics under periodic forcing. Our most important discovery is the non-monotonicity of the period function for the impact oscillator. We have discussed and experimentally verified one consequence of this behavior: the unexpected range of forcing for which $(1:1)$ resonance occurs. Due to the non-monotonicity of the period function, harmonics exist for forcing periods much smaller than those for the pendulum with no barrier. This phenomenon should be explored for other dynamical systems modeling repeated impact phenomena.

Chapter 4

Non-Monotone Period Function for an Impact Oscillator

4.1 Introduction

The study of period functions is important in applied mathematics; especially, to determine the range of resonances with respect to periodic forcing. Most often, as in the free-swinging pendulum, the period function is monotone. Techniques for detecting monotonicity are the subject of much current research (see, for example, [5, 6, 7, 8, 23, 29]). On the other hand, we know of only one example in the literature where a non-monotone period function occurs for a model equation in applied mathematics, that is the whirling pendulum (see [16]).

As demonstrated in the simulations of the previous chapter, the (conservative) dimensionless impact pendulum model

$$\ddot{x} + \sin x + \gamma H(x) x^{\frac{3}{2}} = 0, \tag{4.1}$$

where γ is a positive parameter has a non-monotone period function. In this chapter, we will prove the non-monotonicity of the period functions for the more general differential equation

$$\ddot{x} + f(x) + \gamma H(x) g(x) = 0. \tag{4.2}$$

In section 4.2, we state the precise conditions that we require on the functions f and g for equation (4.2) to have a non-monotone period function. Under these assumptions, we prove in section 4.3 that the period function is decreasing near the rest point at the downward vertical and, as a corollary, the period function is non-monotone. In section 4.4, our non-monotonicity result is illustrated by numerical integration of the impact pendulum model (4.1).

4.2 The Model Equation

We will assume

H1: there exist positive constants K_1 and K_2 such that $f, g : \mathbb{R} \longrightarrow \mathbb{R}$, $f \in C^4((-K_1, K_2)) \cap C^1(\mathbb{R})$ and $g \in C^1(\mathbb{R})$;

H2: $f(0) = f''(0) = 0$, $f'''(0) < 0$, $f(-K_1) = 0$, $f'(-K_1) < 0$ and $xf(x) > 0$ on $(-K_1, 0) \cup (0, K_2)$;

H3: $g'(x) > 0$ on $(0, K_2)$ and $g(0) = g'(0) = 0$; and

H4: for G such that $G'(x) = g(x)$ and $G(0) = 0$, there exists a positive constant M such that the inequality

$$R(x) := \frac{G'(x)^2 - 2G(x)G''(x)}{G'(x)^3} \leq -M$$

is satisfied for $0 < x < K_2$.

We note that **H1** and **H2** imply $f'(0) > 0$, and we define F such that $F'(x) = f(x)$ and $F(0) = 0$.

The differential equation (4.2) is equivalent to the first-order system

$$\begin{aligned} \dot{x} &= y, \\ \dot{y} &= -f(x) - \gamma H(x) g(x), \end{aligned} \tag{4.3}$$

which is in Hamiltonian form with Hamiltonian

$$E(x, y) := \frac{1}{2}y^2 + U(x, \gamma) = \frac{1}{2}y^2 + F(x) + \gamma H(x) G(x). \tag{4.4}$$

Moreover, it has rest points in the phase plane at $(x, y) = (0, 0)$ and $(-K_1, 0)$. We note that for there to be a rest point at $(-K_1, 0)$ no additional requirement on the function g is necessary because the Heaviside function vanishes for negative values of its argument.

System (4.3) has a hyperbolic saddle point at $(-K_1, 0)$; and, there is some number $\gamma_1 > 0$ such that, for $\gamma > \gamma_1$, this saddle point has a corresponding homoclinic orbit surrounding the rest point at the origin and a period annulus containing all other interior orbits. A sample phase portrait for the impact pendulum (4.1) is shown in Fig. 4.1. In general, the energies of the energy level sets surrounded by the homoclinic loop increase from 0 at the origin to $F(-K_1)$ at the homoclinic orbit.

We will prove that if $\gamma > 0$ is sufficiently large, then there is an open interval of energy levels, bounded below by the energy of the origin, for which the period function is decreasing. Since the period function increases near the homoclinic orbit and is C^1 in the punctured region surrounded by the homoclinic orbit, the period function is non-monotone for sufficiently large $\gamma > 0$. We opt for a simple self-contained proof of this result, which can also be obtained using more general results on the first derivatives of period functions (see, for example, [8]).

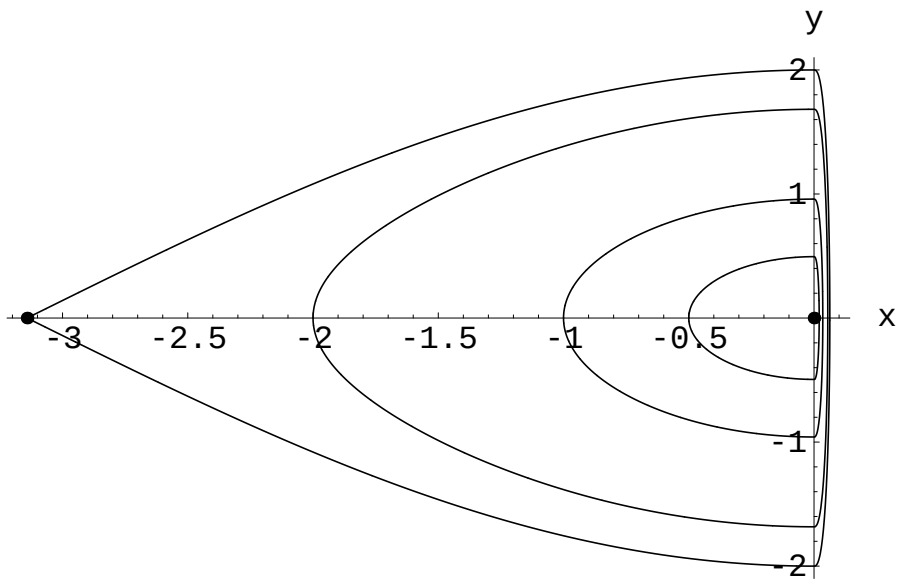

Figure 4.1: Phase portrait for the impact pendulum (4.1) for $\gamma = 5000$.

4.3 The Period Function Near the Origin

By our hypotheses, F is invertible on the interval $(-K_1, 0]$ and $F+\gamma G$ is invertible on $[0, K_2)$. For each energy level E in the range $(0, F(-K_1))$, let $x_-(E) := x \in (-K_1, 0)$ such that $E = F(x)$ and $x_+(E, \gamma) := x \in (0, K_2)$ such that $E = F(x) + \gamma G(x)$. Because $F^{-1}(0) = 0$ and $x_-(E) = F^{-1}(E)$, it follows that $\lim_{E\to 0} x_-(E) = 0$.

Lemma 4.3.1. *There exists $\gamma_2 > \gamma_1$ and a positive constant M such that for U as defined in formula* (4.4)*, we have*

$$W(x,\gamma) := \gamma \frac{(U_x(x,\gamma))^2 - 2U(x,\gamma)U_{xx}(x,\gamma)}{(U_x(x,\gamma))^3} \leq \frac{-M}{2}$$

for all $\gamma > \gamma_2$ and $0 \leq x \leq K_2$.

Proof. We have that $W(x,\gamma) \to R(x)$ as $\gamma \to \infty$ and, by hypothesis **H4**, $R(x) \leq -M$ on $(0, K_2)$. □

Lemma 4.3.2. *The function Q given by*

$$Q(s) := \frac{2F''(s)F(s) - (F'(s))^2}{(F'(s))^3},$$

for $s \neq 0$ and $Q(0) = 0$ is class C^1. Moreover, there exist positive constants E_2 and C such that $Q'(s) < 0$ for all $x_-(E) \leq s < 0$ and $0 < Q(x_-(E)) \leq C\sqrt{E}$ for all $E < E_2$.

Proof. The Taylor expansion of the function F at the origin has the form

$$F(s) = \frac{\lambda^2}{2}s^2 - \frac{\mu^2}{24}s^4 + O(s^5),$$

where λ and μ are positive constants. By substituting this series into the formula for Q and simplifying the resulting expression, we see that Q has a removable singularity at $s = 0$. The regularized Taylor series of Q at $s = 0$ has the form

$$Q(s) = -c^2 s + O(s^3),$$

where c is a positive constant. In particular, $Q'(0) = -c^2$.

Thus, there exists $\delta > 0$ such that $-2c^2 \leq Q'(s) \leq -c^2/2$ for all $s \in (-\delta, 0)$. Also, since $x_-(E) \to 0^-$ as $E \to 0^+$, there exists E_1 such that $-\delta < x_-(E) \leq 0$ for all $E < E_1$. So, for all $E < E_1$ and $x_-(E) < s < 0$, we have $Q'(s) < 0$.

By the Mean Value Theorem, there is some $\xi \in (0, s)$ and a positive constant c such that

$$Q(s) = Q(s) - Q(0) = |\, Q'(\xi)||\, s| \leq 2c^2|\, s|$$

for all $s \in (-\delta, 0)$. So, $Q(x_-(E)) \leq 2c^2|\, x_-(E)|$ for $E < E_1$.

Using the Taylor expansion of F, we also have

$$\lim_{E\to 0^+} \frac{|\, x_-(E)|}{\sqrt{E}} = \lim_{E\to 0^+} \frac{-x_-(E)}{\sqrt{F(x_-(E))}} = \lim_{s\to 0^-} \frac{-s}{\sqrt{\frac{\lambda^2}{2}s^2 + O(s^4)}} = \sqrt{\frac{2}{\lambda^2}}\,.$$

Hence, there exists $E_2 < E_1$ such that $|x_-(E)| \leq 2\sqrt{E}/\sqrt{\lambda^2}$ for all $E < E_2$.

Combining our results, we have that

$$Q(x_-(E)) \leq 2c^2 |x_-(E)| \leq \frac{2c}{\sqrt{\lambda^2}}\sqrt{E} = C\sqrt{E}$$

for all $E < E_2$, where we have consolidated constants. □

Let P be the period function on the period annulus surrounded by the homoclinic loop for system (4.2). The period for the orbit at energy level E is given by $P(E, \gamma)$, and the derivative of P with respect to E is denoted $P'(E, \gamma)$.

The next theorem is our main result.

Theorem 4.3.3. *Let γ_2 be the number in Lemma 4.3.1. For fixed $\gamma > \gamma_2$, there exists a positive number E_* such that $P'(E, \gamma) < 0$ for all $0 < E < E_*$.*

Proof. Fix $\gamma > \gamma_2$. For simplicity, we will suppress γ in the expressions $U(x, \gamma), x_+(e, \gamma)$ and $P(E, \gamma)$.

Using the Hamiltonian given in equation (4.4) and integrating along orbits, we arrive at the familiar formula for the period of the orbit at energy level E (see [4]):

$$P(E) = \frac{2}{\sqrt{2}} \int_{x_-(E)}^{x_+(E)} \frac{dx}{\sqrt{E - U(x)}} \, .$$

The change of variables $s = h(x)$, where $h(x) = \operatorname{sgn}(x)\sqrt{2U(x)}$, transforms the integral into

$$P(E) = \frac{2}{\sqrt{2}} \int_{-\sqrt{2E}}^{\sqrt{2E}} \frac{s}{U'(h^{-1}(s))\sqrt{E - \frac{s^2}{2}}} \, ds \, .$$

After another change of variables, $s = \sqrt{2E}\sin\theta$, the period function is represented by

$$P(E) = 2\int_{-\frac{\pi}{2}}^{\frac{\pi}{2}} \frac{d\theta}{h'(h^{-1}(\sqrt{2E}\sin\theta))} = 2\int_{-\frac{\pi}{2}}^{\frac{\pi}{2}} (h^{-1})'(\sqrt{2E}\sin\theta)\, d\theta. \tag{4.5}$$

By differentiating and splitting the integral in two pieces, we have

$$\begin{aligned} P'(E) &= \sqrt{\tfrac{2}{E}} \int_{-\frac{\pi}{2}}^{0} (h^{-1})''(\sqrt{2E}\sin\theta)\sin\theta\, d\theta \\ &\quad + \sqrt{\tfrac{2}{E}} \int_{0}^{\frac{\pi}{2}} (h^{-1})''(\sqrt{2E}\sin\theta)\sin\theta\, d\theta \\ &= I + II. \end{aligned}$$

Lemma 4.3.4. *Let E_2 be as in Lemma 4.3.2. If $0 < E < E_2$, then $0 < I < C_1$.*

Proof. Rewrite I as

$$I = \sqrt{\frac{2}{E}} \int_{-\frac{\pi}{2}}^{0} (h^{-1})''(h(\tau(\theta)))\sin\theta\, d\theta,$$

where $\tau(\theta) := F^{-1}(E\sin^2\theta)$, which is a well-defined function because F is restricted to $(-K_1, 0]$. Using the formula $(h^{-1})''(h(s)) = -h''(s)/(h'(s))^3$ and making the change of variables $s = \tau(\theta)$, we have

$$I = \sqrt{\frac{2}{E}} \int_{x_-(E)}^{0} \frac{-h''(s)\sin(\tau^{-1}(s))}{(h'(s))^3 \tau'(\tau^{-1}(s))}\, ds\ .$$

Substituting in the formula

$$\tau^{-1}(s) = \sin^{-1}(-\sqrt{F(s)/E}\,)$$

and using the definitions of h and τ, the last expression for I simplifies to

$$I = \frac{1}{\sqrt{2}E} \int_{x_-(E)}^{0} Q(s) \frac{-F'(s)}{\sqrt{E - F(s)}}\, ds\ .$$

By Lemma 4.3.2 and the inequalities $Q(s) > 0$ and $F'(s) < 0$ on $(x_-(E), 0)$, it follows that I is positive and

$$I \le \frac{Q(x_-(E))}{\sqrt{2}E} \int_{x_-(E)}^{0} \frac{-F'(s)}{\sqrt{E - F(s)}}\, ds = \frac{\sqrt{2}Q(x_-(E))}{\sqrt{E}} \le \frac{\sqrt{2}\, C\sqrt{E}}{\sqrt{E}} = C_1\ ,$$

where we have consolidated constants. □

Lemma 4.3.5. *Integral II is negative and $|\,II| > C_2/(\gamma\sqrt{E}\,)$.*

Proof. By defining $\tau(\theta) := U^{-1}(E\sin^2\theta)$ and proceeding as in Lemma 4.3.4, we express II in the form

$$II = \frac{1}{\sqrt{2}E}\int_0^{x_+(E)} \frac{(U'(s))^2 - 2U(s)U''(s)}{(U'(s))^3}\frac{U'(s)}{\sqrt{E-U(s)}}\,ds\ .$$

By Lemma 4.3.1 and the inequality $U'(s) \geq 0$ on $(0, x_+(E))$, the integrand is always negative. Thus, $II < 0$ and

$$|\,II| > \frac{M}{2\sqrt{2}E\gamma}\int_0^{x_+(E)} \frac{U'(s)}{\sqrt{E-U(s)}}\,ds = \frac{2M\sqrt{E}}{2\sqrt{2}E\gamma} = \frac{C_2}{\gamma\sqrt{E}}\,,$$

where we have consolidated constants. □

To complete the proof of the theorem, we choose $E_* = \min(E_2, C_2^2/(\gamma^2 C_1^2))$ so that $P'(E,\gamma) = I + II < 0$ whenever $0 < E < E_*$. □

Corollary 4.3.6. *Let γ_2 be as in Theorem 4.3.3. If $\gamma > \gamma_2$, then the period function for system (4.2) is non-monotone and has at least one critical point in the interval $[E_*, F(-K_1))$.*

Corollary 4.3.7. *Let γ_2 be as in Theorem 4.3.3. If $\gamma > \gamma_2$ and $x_c > 0$ is sufficiently small, then the period function for the system*

$$\ddot{x} + f(x) + \gamma H(x - x_c)g(x - x_c) = 0 \tag{4.6}$$

is non-monotone and has at least two critical points.

Proof. Let $T(x_0, x_c)$ be the period of the orbit with initial conditions $x(0) = x_0$ and $\dot{x}(0) = 0$ for equation (4.6) and define

$$T(0, x_c) = \lim_{x_0 \to 0} T(x_0, x_c).$$

Since T is continuous and the function $x_0 \mapsto T(x_0, 0)$ is decreasing near the origin, there exists $\bar{x}_0$ near 0 such that $T(\bar{x}_0, 0) < T(0, 0)$. Hence, $T(\bar{x}_0, \bar{x}_c) < T(0, 0)$ for $\bar{x}_c$ sufficiently small.

Alternatively, in a neighborhood of the origin, for $x_c > 0$, the period function $T(x_0, \bar{x}_c)$ must coincide with the period function of $\ddot{x} + f(x) = 0$, which is increasing near the origin.

Because the periods of periodic orbits are unbounded in a neighborhood of the homoclinic loop boundary of the period annulus under consideration, we have the desired result. □

4.4 The Impact Pendulum

The non-dimensional system $\ddot{x} + \sin x + \gamma H(x) x^{\frac{3}{2}} = 0$ is a Hertzian contact model (see [9, 13]) for an undamped unforced pendulum striking an elastic barrier at its downward vertical position. The constant γ corresponds to the elastic modulus of the barrier (see [19]).

The functions $f(x) = \sin x$ and $g(x) = x^{\frac{3}{2}}$ satisfy the assumptions in section 4.2 for Theorem 4.3.3, which states that there exists a region near the rest point at the barrier where the period function is decreasing. Using numerical integration techniques with $\gamma = 3.57 \times 10^8$ (an approximate value for an aluminum barrier), we are able to integrate the system numerically and graph its period function.

A plot of the period function near $E = 0$ is given in Fig. 4.2, which confirms that the period function is decreasing near $E = 0$. The interval of decrease is small in this case because γ is large.

Numerical experiments suggest that a version of the decreasing period phenomenon

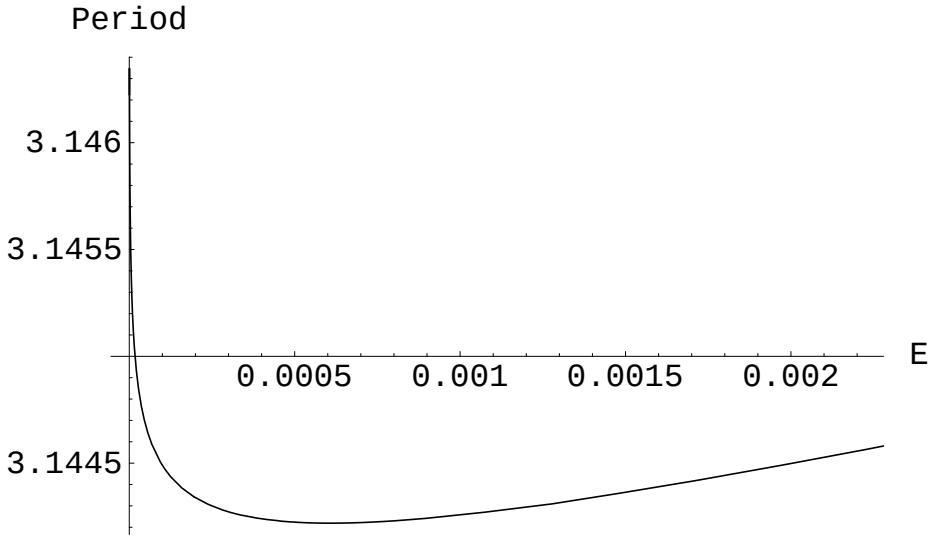

Figure 4.2: Period function for the impact pendulum (4.1) with $\gamma = 3.57 \times 10^8$.

persists in case the wall is positioned at some positive angle relative to the downward vertical. The Hertzian contact model for the impact pendulum with wall angle $x_c > 0$ is

$$\ddot{x} + \sin x + \gamma H(x - x_c)(x - x_c)^{\frac{3}{2}} = 0. \tag{4.7}$$

Theorem 4.3.3 does not apply to the impact pendulum in this case because our hypotheses are not satisfied. In fact, due to the smoothness of the period function and its positive derivative in the region of small oscillation with no impacts, there must exist an interval containing the contact point on which the period function increases. Our numerical experiments verify this fact and suggest that the period function will decrease for an interval corresponding to more energetic impacts, reach a minimum value, and then increase as the energies of the periodic orbits approach the energy of the homoclinic loop. This scenario is illustrated in Fig. 4.3.

A natural prediction (cf. [3, Ch. 5]) is that harmonic motions of the periodically forced and damped pendulum with impacts will correspond to low-order resonances

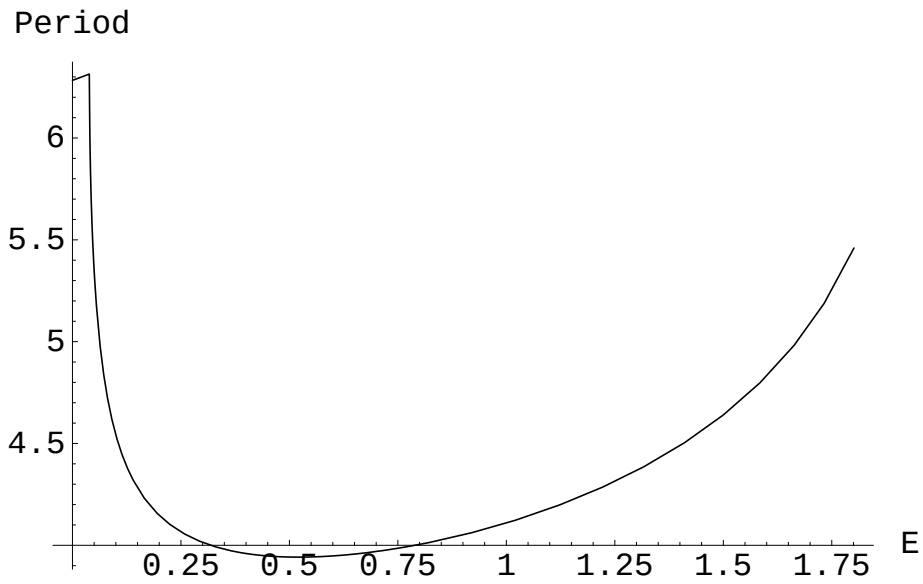

Figure 4.3: Period function for the impact pendulum (4.7) with $x_c = 0.281$ and $\gamma = 3.57 \times 10^8$.

between the forcing period and the available periods of the conservative impact pendulum studied in this chapter. In experiments, where only relatively small oscillations are feasible, the interval of available periods is the interval corresponding to the local maximum and local minimum in Fig. 4.3. By approximating these values, the range of $(1:1)$-period locking (harmonic motions) has been predicted and verified by physical experiments in the previous chapter.

Chapter 5

Oscillator Excitation

5.1 Introduction

An important problem in engineering is finding methods to excite non-linear systems to higher energy levels. In the case of an electronic circuit, the goal could be to excite the system into a chaotic regime or to energy levels so high that the dynamics of the system are radically altered. This has numerous military applications. For example, if it is possible to excite the electronic system of a hostile tracking and guidance system to an energy outside of its intended operational envelope, then the likelihood of the system failing its mission is greatly increased. For applications of this concept, see [14] where the authors have implemented this idea using specifically constructed circuits.

For the purposes of our work, we are restricting the underlying dynamical system to those of classical Hamiltonian form, that is

$$\ddot{x} + V'(x) = 0,$$

where $x \in \mathbb{R}$ is the state variable, the dots represent time derivatives and $V(x)$ is the potential energy. Expressing this as a first order system, we have

$$\begin{aligned} \dot{x} &= v \\ \dot{v} &= -V'(x), \end{aligned}$$

or as a vector equation

$$\dot{w} = f(w). \tag{5.1}$$

The underlying idea is that we are only allowed to record a time series of the state variable for the unknown system (5.1). From this time series, we will provide a method for determining an excitation function $g(t)$ that produces an increase in system energy. We will then discuss the feasibility of such a procedure when damping is included. Finally, we show numerical simulations of the method in action for example systems.

5.2 Definitions and Assumptions

For simplicity, we now make several definitions and assumptions that will be used throughout this chapter.

- We define the pseudo-period of an orbit γ at a point A in $\mathbb{R}^2$, to be the backward time for γ to return to the ray, called the return-ray, connecting the origin and A.

- We define the pseudo-phase of an orbit γ as the phase of γ over the previous pseudo-period.

- We assume there exists an annulus of stable periodic orbits for the free system (5.1) extending from a minimum energy level at the origin to some critical

energy level which we call E^*.

- We assume f in equation (5.1) is Lipschitz with constant L.

5.3 Preliminaries

Let us examine the differential equations

$$\dot{w} = f(w) + \epsilon g(t), \tag{5.2}$$

$$\dot{y} = f(y), \tag{5.3}$$

with identical initial conditions, and flows in the phase plane that transversally cross every line passing through the origin.

Lemma 5.3.1. *For all $t > 0$,*

$$|w(t) - y(t)| \leq \epsilon\, e^{Lt} \int_0^t |g(s)|\, ds = \epsilon e^{Lt} G(t),$$

where L is the Lipschitz constant of f, $w(t) \in \mathbb{R}$, and $y(t) \in \mathbb{R}$ are the solutions of (5.2) *and* (5.3) *respectively.*

Proof. Let $u(t) = w(t) - y(t)$. Then $\dot{u}(t) = f(w(t)) - f(y(t)) + \epsilon g(t)$ and

$$u(t) - u(0) = \int_0^t f(w(s)) - f(y(s)) + \epsilon g(s)\, ds.$$

Taking absolute values and moving those inside the integrals, we have

$$\begin{aligned} |u(t) \quad| &\leq \epsilon \int_0^t |g(s)|\, ds + \int_0^t |f(w(s)) - f(y(s))|\, ds \\ &\leq \epsilon \int_0^t |g(s)|\, ds + \int_0^t L|u(s)|\, ds. \end{aligned}$$

Applying Gronwall's Inequality, we have

$$|u(t)| \leq \epsilon e^{\int_0^t L\, ds} \int_0^t |g(s)|\, ds = \epsilon\, e^{Lt} \int_0^t |g(s)|\, ds.$$

□

Lemma 5.3.2. *For sufficiently small $\epsilon > 0$, if P and T are the pseudo-periods of* (5.2) *and* (5.3) *respectively with initial condition $\xi = (a, b)$, then*

$$|P - T| \leq \epsilon M,$$

up to order ϵ where M does not depend on ϵ or P.

Proof. For initial conditions $\xi = (a, b) \neq (0, 0)$, let $u(t, \xi, \epsilon)$ be the solution to (5.2) for $\epsilon \geq 0$. We define the return ray as all points (x_1, x_2) in $\mathbb{R}^2$ such that $bx_1 - ax_2 = 0$, $ax_1 > 0$ and $bx_2 > 0$. Hence [1]$bu_1(T, \xi, 0) - au_2(T, \xi, 0) = 0$, where T is the period for system (5.2) with $\epsilon = 0$. Also, for small $\epsilon > 0$, there exists a solution $u(t, \xi, \epsilon)$ and a minimum positive value P, which satisfies $bu_1(P, \xi, \epsilon) - au_2(P, \xi, \epsilon) = 0$.

We now define $F(t, \xi, \epsilon) = bu_1(t, \xi, \epsilon) - au_2(t, \xi, \epsilon)$. Thus, $F(T, \xi, 0) = 0$ and using the transverse flow condition,

$$F_t(T, \xi, 0) = bu_{1}(T, \xi, 0) - au_{2}(T, \xi, 0) = bf_1(\xi) - af_2(\xi) \neq 0.$$

By the Implicit Function Theorem, there exists $\eta(\xi, \epsilon)$ such that $F(\eta(\bar{\xi}, \epsilon), \bar{\xi}, \epsilon) = 0$ for all $(\bar{\xi}, \epsilon)$ near $(\xi, 0)$.

Differentiating F with respect to ϵ,

$$F_t(\eta(\xi, \epsilon), \xi), \epsilon)\eta_\epsilon(\xi, \epsilon) + F_\epsilon(\eta(\xi, \epsilon), \xi, \epsilon) = 0$$

and hence,

$$\eta_\epsilon(\xi, \epsilon) = \frac{-F_\epsilon}{F_t}(\eta_\epsilon(\xi, \epsilon), \xi, \epsilon). \tag{5.4}$$

After differentiating $F(T, \xi, \epsilon)$ with respect to ϵ, we have

$$F_\epsilon(T, \xi, 0) = bu_{1\epsilon}(T, \xi, 0) - au_{2\epsilon}(T, \xi, 0). \tag{5.5}$$

[1]Numeric subscripts represent components of a vector function, non-numeric subscripts denote partial derivatives

Let $\Phi(t)$ be the fundamental matrix solution of $\dot{u}_\epsilon = Df(u)u_\epsilon$, then the solution of the variational equation $\dot{u}_\epsilon = Df(u)u_\epsilon + g(t)$ is

$$u_\epsilon(T,\xi,0) = \Phi(T)u_\epsilon(0,\xi,0) + \Phi(T)\int_0^T \Phi^{-1}(s)g(s)\,ds = \Phi(T)\int_0^T \Phi^{-1}(s)g(s)\,ds$$

by the variation of parameters method. Plugging into (5.5) and then (5.4), we have $F_\epsilon(T,\xi,0) = (b,-a)\cdot\Phi(T)\int_0^T \Phi^{-1}(s)g(s)\,ds$ and

$$|\eta_\epsilon(\xi,0)| \leq \frac{|(b,-a)\cdot\Phi(T)\int_0^T \Phi^{-1}(s)g(s)\,ds|}{|(b,-a)\cdot f(\xi)|} \leq M, \tag{5.6}$$

where the boundedness of the middle expression is due to the transversality of f and the return ray. Expanding η about $\epsilon = 0$, we have $P = T + \epsilon\eta_\epsilon(\xi,0) + O(\epsilon^2)$. Using inequality (5.6) and gathering terms, we arrive at

$$|P - T| \leq \epsilon|\eta_\epsilon(\xi,0)| \leq \epsilon M \tag{5.7}$$

up to order epsilon. □

5.4 Main Result

We are concerned with the dimensionless system

$$\ddot{x} + V'(x) = \epsilon g(t) \tag{5.8}$$

where V is Lipschitz and g is bounded and continuous. We also require the system to be of classical Hamiltonian form. Thus, the energy of the system is given by $E(x,\dot{x}) = \frac{\dot{x}^2}{2} + V(x)$. We also require the system be periodic for $\epsilon = 0$ and every periodic orbit must cross transversally through every line containing the origin in the phase plane. As a first order system, this becomes

$$\begin{aligned} \dot{x} &= v, \\ \dot{v} &= -V'(x) + \epsilon g(t). \end{aligned} \tag{5.9}$$

Expressing (5.9) as a vector equation, we have

$$\dot{w} = f(w) + \epsilon \hat{g}(t), \tag{5.10}$$

where $w = (x, v)$, $\hat{g}(t)$ is the vector function with 0 in the first component, and $g(t)$ in the second, and f is Lipschitz with constant L.

Theorem 5.4.1. *For ϵ sufficiently small, the energy of system (5.8) will increase for $g(t) = \bar{x}'(t)$ over one forward pseudo-period, P, where $\bar{x}(t)$ is the time series of system (5.8) with $\epsilon = 0$ recorded over one previous period, T, and extended to a T-periodic function on all of $\mathbb{R}$.*

Proof. Differentiating the energy once with respect to time and substituting (5.9), we have

$$\frac{dE}{dt}(x, v) = v\dot{v} + V'(x)\dot{x} = v(-V'(x) + \epsilon g(t)) + V'(x)v = \epsilon v g(t).$$

Let ϵ_1 be such that lemma (5.3.2) holds for all $\epsilon \leq \epsilon_1$. Then P is well defined and the change in energy over one forward pseudo-period, P, is

$$\Delta E = \int_0^P \epsilon v(s, \epsilon) g(s)\, ds, \tag{5.11}$$

where both v and P depend on g, ϵ and the initial condition ξ.

Let us choose $g(t) = \bar{x}'(t) = \bar{v}(t)$. We assume $P \geq T$, which yields

$$\begin{aligned} \frac{\Delta E}{\epsilon} &= \int_0^T v(t, \epsilon)\bar{v}(t)\, dt + \int_T^P v(t, \epsilon)\bar{v}(t)\, dt & (5.12) \\ &= \int_0^T (v - \bar{v} + \bar{v})\bar{v}\, dt + \int_T^P (v - \bar{v} + \bar{v})\bar{v}\, dt, & (5.13) \end{aligned}$$

where we have suppressed the dependence on t and ϵ inside the integrals on the last line.

Taking absolute values and applying the triangle law, this becomes

$$\frac{\Delta E}{\epsilon} \geq \int_0^T |\bar{v}|^2\,dt - \int_0^T |v-\bar{v}||\bar{v}|\,dt - \int_T^P |v-\bar{v}||\bar{v}|\,dt - \int_T^P |\bar{v}|^2\,dt.$$

Using system (5.10) and lemma (5.3.1), we also have

$$|v-\bar{v}| \leq |f(w)-f(\bar{w})| + \epsilon g(t) \leq L|w-\bar{w}| + \epsilon g(t) \leq \epsilon(e^{Lt}\bar{x}(t) + \bar{v}(t)) = \epsilon B(t).$$

After combining the above inequalities and applying Holder's inequality,

$$\begin{aligned}
\frac{\Delta E}{\epsilon} &\geq C^2 - \epsilon C\big[\int_0^T B^2(t)\,dt\big]^{1/2} \\
&\quad -\epsilon\big[\int_T^P B^2(t)\,dt\big]^{1/2}\big[\int_0^{P-T} |\bar{v}|^2\,dt\big]^{1/2} - \int_0^{P-T} |\bar{v}|^2\,dt \\
&\geq C^2 - \frac{C^2}{4} - \epsilon\big[C\big(\int_0^T B^2(t)\,dt\big)^{1/2} + \frac{C}{2}\big(\int_T^{T+\epsilon_1 M} B^2(t)\,dt\big)^{1/2}\big]
\end{aligned}$$

for all $\epsilon \leq \epsilon_2 \leq \epsilon_1$ such that

$$\int_0^{\epsilon_2 M} |\bar{v}|^2\,dt \leq \frac{1}{4}\int_0^T |\bar{v}|^2 = \frac{C^2}{4},$$

where M is defined in inequality (5.6) and C is the L^2 norm of $\bar{v}(t)$ on the interval $0 \leq t \leq T$. Choosing $\epsilon_3 \leq \epsilon_2$ such that

$$\epsilon_3 < \frac{3C}{4(\int_0^T B^2(t)\,dt)^{1/2} + 2(\int_T^{T+\epsilon_2 M} B^2(t)\,dt)^{1/2}},$$

we have that $\Delta E > 0$ for all $\epsilon \leq \epsilon_3$. If $P < T$, then replace T with P in every integral and the inequalities still hold. □

5.5 Damping

While we treat the system with no external excitation as undamped, the introduction of the excitation function, $\epsilon g(t)$, could introduce damping into the system. The first-order system with forcing and viscous damping is

$$\begin{aligned} \dot{x} &= v \\ \dot{v} &= -V'(x) + \epsilon(g(t) - \alpha v), \end{aligned} \tag{5.14}$$

where α is the damping coefficient. The corresponding change in energy is given by

$$\frac{dE}{dt}(x,v) = v\dot{v} + V'(x)\dot{x} = v(-V'(x) + \epsilon(g(t) - \alpha v)) + V'(x)v = \epsilon v g(t) - \epsilon\alpha v^2. \tag{5.15}$$

We must then analyze the effect of the damping term over one pseudo-period. The energy change due to damping will be present not only in the extra term, but also in the estimates given in lemmas (5.3.1) and (5.3.2). Similar results will hold due to the smoothness of the differential equation for ϵ sufficiently small.

The energy change over one period due to the last term in equation (5.15) is

$$\frac{\Delta E}{\epsilon} = -\alpha \int_0^P v^2(t)\, ds.$$

Thus, if the damping constant α is sufficiently small as well, the system should increase in energy for the choice of excitation function given in the previous section.

5.6 Application

In this section we will outline an algorithm for increasing the energy of Classical Hamiltonian systems in an annulus of periodic orbits and provide numerical results using the algorithm with example systems. The unforced system has the form

$$\ddot{x} + V'(x) = 0. \tag{5.16}$$

We record the time trace of the state variable $x(t)$ with initial condition on the positive x-axis in the phase plane until it returns to the positive x-axis at time T. We

then apply an external forcing function $\epsilon g(t)$ to system (5.16). We set $g(t) = x'(t)$ extended to a T-periodic function on all of $\mathbb{R}$. We then record the time trace of the system

$$\ddot{x} + V'(x) = \epsilon g(t) \tag{5.17}$$

until the orbit returns to the positive x-axis in the phase plane. The orbit will return to the positive x-axis for ϵ small by the stability of the periodic orbits.

By the proof of the main result, the energy of the system must increase for ϵ small. To continue, we set $g(t) = 0$ and record the time trace of system (5.17) until the orbit returns to the positive x-axis in the phase plane. We then repeat the process by setting $g(t) = x'(t)$ and applying the forcing function for one forward pseudo-period. Each application of this procedure will increase the system energy for ϵ small. The desired energy level is called the critical energy level and necessarily occurs at an energy level less than the least energy value beyond the annulus of stable periodic orbits.

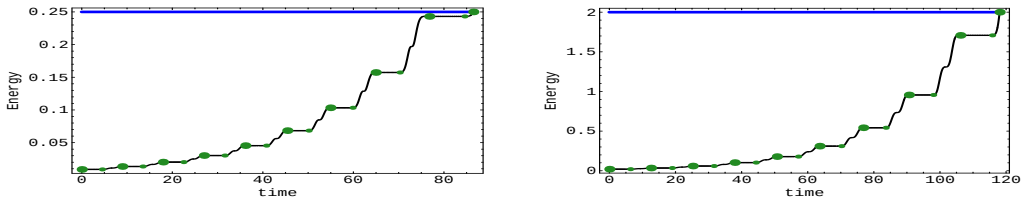

Figure 5.1: Plots of energy curves over time. The critical energy is represented by the horizontal line. The large points correspond to the beginning of each iteration of the algorithm while the smaller points are the transitions between the free oscillator and the externally forced oscillator ($g(t) \equiv 0$ and $g(t) = x'(t)$ respectively). The left figure is for the system $\ddot{x} + \sin x = 0$ with initial conditions $x(0) = 0.2$, $x'(0) = 0$. The right figure is for the system $\ddot{x} + x^3 - 3x^2 + 2x = 0$ with initial conditions $x(0) = 0.1$, $x'(0) = 0$.

The plots shown in Fig. 5.1 are numerical results obtained by applying the above algorithm with $\epsilon = 0.1$ to example systems using code written in Mathematica 3.0.

The critical level for each corresponds to the energy of the homoclinic loop bounding the annulus of periodic orbits.

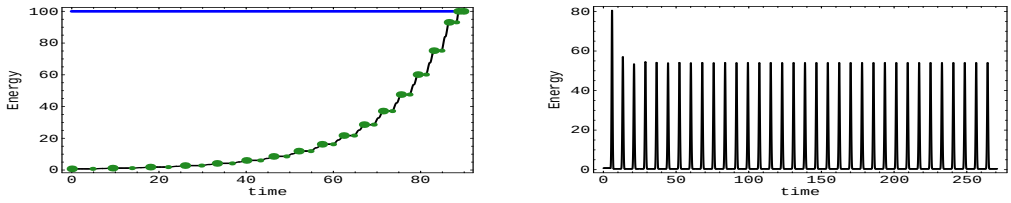

Figure 5.2: Plots of energy curves over time. The critical energy is represented by the horizontal line. The large points correspond to the beginning of each iteration of the algorithm while the smaller points are the transitions between the free oscillator and the externally forced oscillator ($g(t) \equiv 0$ and $g(t) = x'(t)$ respectively). Both figures are for the system $\ddot{x} + x^3 + x = 0$ with initial conditions $x(0) = 1$, $x'(0) = 0$. The left figure is for $\epsilon = 0.1$ while the right figure is for $\epsilon = 15$.

The plots shown in Fig. 5.2 are numerical results obtained by applying the above algorithm for small and large choices of ϵ. The annulus of stable periodic orbits of system $\ddot{x} + x^3 + x = 0$ exists for all energy values, thus the critical energy is chosen independent of the system. For this example, we have chosen a critical energy level of 100. In the left figure, the energy increases to the critical energy level. However, when the size of ϵ is increased from $\epsilon = 0.1$ to $\epsilon = 15$, the algorithm fails and the energy cannot be increased to the critical energy level.

The result of these simulations supports the main result. That is, the energy of a Classical Hamiltonian oscillator in a neighborhood of stable periodic orbits can be increased by applying a forcing function determined from a time trace recorded over one previous pseudo-period provided the magnitude of forcing is kept sufficiently small.

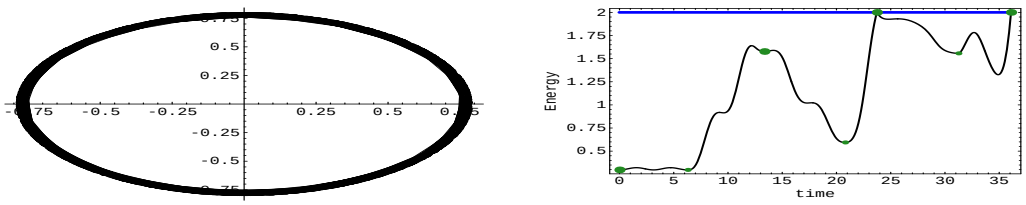

Figure 5.3: The left figure is a plot in the phase plane of the system $\ddot{x}+\sin x+0.1\dot{x} = 0.1\sin(t+500.167)$ with initial conditions $x(0) = 0.791601$, $x'(0) = 0$. The right figure is a plot of the energy of the system after applying the algorithm with the same initial conditions and $\epsilon = 0.5$.

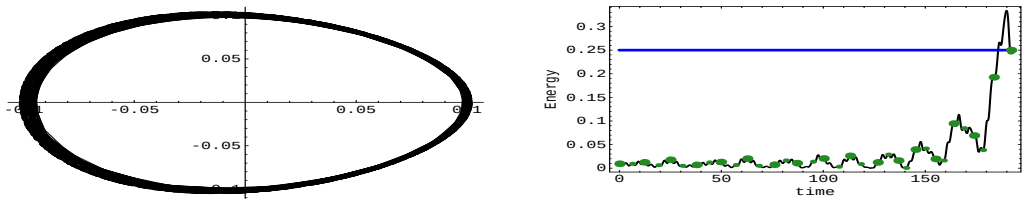

Figure 5.4: The left figure is a plot in the phase plane of the system $\ddot{x} + x^3 - 3x^2 + 2x + 0.03\dot{x} = 0.1\sin(t + 504.264)$ with initial conditions $x(0) = 0.102347$, $x'(0) = 0$. The right figure is a plot of the energy of the system after applying the algorithm with the same initial conditions and $\epsilon = 0.2$.

5.7 Internal Damping and Forcing

Although the proof of the main result does not apply to systems with internal damping and forcing, applying the same algorithm results in energy increases for many of these systems as well. To model this, we use systems of the form discussed in the previous section, only we include small damping and forcing terms. While the proof of the main result requires periodic motion, in practice, we can apply the general technique to nearly periodic motion.

The plots shown in Figs. 5.3, 5.4 show that the algorithm can succeed in increasing the energy even in the presence of damping and forcing. The plots shown in Fig. 5.5 illustrate that with damping and forcing included, small ϵ does not guarantee an increase in energy. This is due to the loss of energy from damping that increases as the energy increases. For each critical energy level desired, there will be a minimum

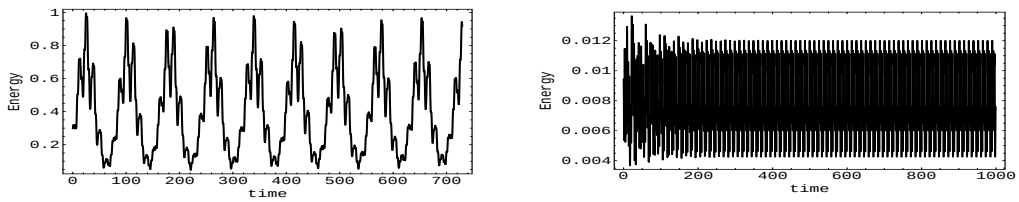

Figure 5.5: The left figure is a plot of the energy of the system $\ddot{x} + \sin x + 0.1\dot{x} = 0.1\sin(t + 500.167)$ with initial conditions $x(0) = 0.791601$, $x'(0) = 0$ after applying the algorithm with $\epsilon = 0.2$. The right figure is a plot of the energy of the system $\ddot{x}+x^3-3x^2+2x+0.03\dot{x} = 0.1\sin(t+504.264)$ with initial conditions $x(0) = 0.102347$, $x'(0) = 0$ after applying the algorithm with $\epsilon = 0.1$.

magnitude of ϵ required for the energy gain to offset the increased energy loss. This is in conflict with the small epsilon required in the proof of the main result. For the example systems shown in this section, there is an interval of values for ϵ that meet both criteria.

5.8 Higher Dimensions

We can modify the results from the previous sections to include systems with more than one degree of freedom. We still require a Classical Hamiltonian system. Thus, the system of concern is of the form

$$\ddot{x} + \nabla V(x) = \epsilon f(t), \tag{5.18}$$

where $x \in \mathbb{R}^n$, $V(x)$ is the potential, $f(t)$ is continuous, and $\epsilon \geq 0$. We also require the existence of a stable periodic orbit, Σ, for $\epsilon = 0$. Let $x(t, \epsilon, \zeta)$ be the solution to system (5.18) with initial conditions $\zeta = (x_0, v_0)$ where $x(0, \epsilon, \zeta) = x_0$ and $\dot{x}(0, \epsilon, \zeta) = v_0$. Let $T(\zeta)$ be the period for initial conditions $\zeta \in \Sigma$ and $\epsilon = 0$.

Theorem 5.8.1. *For sufficiently small ϵ, system* (5.18) *will increase in energy over the time interval $0 \leq t \leq T(\zeta)$ for initial conditions $\zeta \in \Sigma$ and $f(t) = \dot{x}(t, 0, \zeta)$.*

Proof. The energy of system (5.18) is given by $E(x, \dot{x}) = \frac{1}{2}\langle \dot{x}, \dot{x} \rangle + V(x)$ and the change in energy with respect to time is

$$\frac{dE}{dt} = \langle \ddot{x}(t), \dot{x}(t) \rangle + \langle \nabla V(x(t)), \dot{x}(t) \rangle,$$

where $\langle \cdot, \cdot \rangle$ represents the inner product. Substituting system (5.18) and simplifying, we have

$$\frac{dE}{dt} = \langle -\nabla V(x(t)) + \epsilon f(t), \dot{x}(t) \rangle + \langle \nabla V(x(t)), \dot{x}(t) \rangle = \epsilon \langle f(t), \dot{x}(t) \rangle.$$

Thus, the total change in energy for $0 \leq t \leq T(\zeta)$ along the orbit with initial conditions ζ is given by

$$\Delta E = \epsilon \int_0^{T(\zeta)} \langle \dot{x}(t, 0, \zeta), \dot{x}(t, \epsilon, \zeta) \rangle \, dt.$$

Substituting $\dot{x}(t, \epsilon, \zeta) = \dot{x}(t, 0, \zeta) + O(\epsilon)$ from lemma (5.3.1) results in

$$\Delta E = \epsilon \int_0^{T(\zeta)} \langle \dot{x}(t, 0, \zeta), \dot{x}(t, 0, \zeta) \rangle + \langle \dot{x}(t, 0, \zeta), O(\epsilon) \rangle \, dt.$$

By taking absolute values and applying the triangle inequality, we have

$$\frac{\Delta E}{\epsilon} \geq \int_0^{T(\zeta)} \langle \dot{x}(t, 0, \zeta), \dot{x}(t, 0, \zeta) \rangle \, dt - |O(\epsilon)|.$$

So, for ϵ sufficiently small, $\Delta E > 0$. □

5.9 Simulations in Higher Dimensions

The system of concern is the two degree of freedom system

$$\begin{aligned} \ddot{x} &= \frac{-x}{(x^2 + y^2)^{3/2}} \\ \ddot{y} &= \frac{-y}{(x^2 + y^2)^{3/2}}, \end{aligned} \tag{5.19}$$

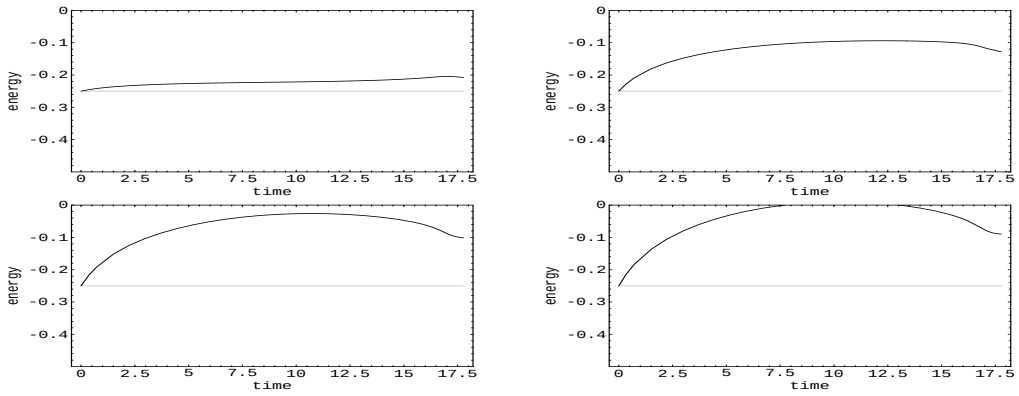

Figure 5.6: Plots of energy versus time with initial conditions $x(0) = 0, y(0) = 1, \dot{x}(0) = -1$ and $\dot{y}(0) = 1/\sqrt{2}$. The plots correspond to $\epsilon = 0.01, 0.05, 0.07, 0.08$ moving from left to right and top to bottom.

which models the motion of a dimensionless binary system moving in three-dimensional space. For a more in-depth analysis of this system, see [3]. The energy of system (5.19) is given by

$$H(x, y) = \frac{1}{2}(\dot{x}^2 + \dot{y}^2) - \frac{1}{\sqrt{x^2 + y^2}},$$

where the region of periodic orbits corresponds to the region with negative energies.

To apply the algorithm outlined in previous sections, we record the time-trace of the system for one period and then apply the recorded data as the forcing function. This results in a system, with forcing included, of the form

$$\begin{aligned} \ddot{x} &= \frac{-x}{(x^2 + y^2)^{3/2}} + \epsilon g_1 \\ \ddot{y} &= \frac{-y}{(x^2 + y^2)^{3/2}} + \epsilon g_2, \end{aligned} \tag{5.20}$$

where g_1 and g_2 are the time derivatives of the recorded state variables, x and y respectively, over one unperturbed periodic orbit. System (5.20) is then integrated forward in time.

The plots shown in Fig. 5.6 and Fig. 5.7 show energy versus time for system (5.20) with initial conditions in the periodic regime for various choices of ϵ. The max-

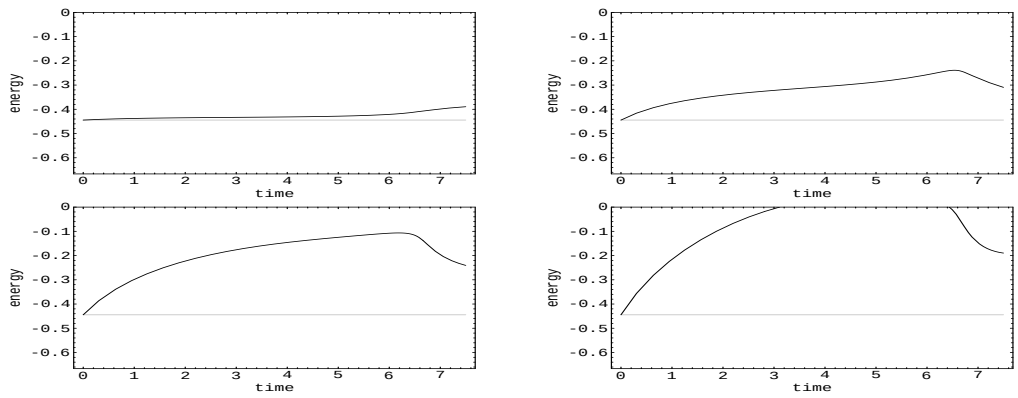

Figure 5.7: Plots of energy versus time with initial conditions $x(0) = 0, y(0) = 1, \dot{x}(0) = -3/4$ and $\dot{y}(0) = \sqrt{79}/12$. The plots correspond to $\epsilon = 0.01, 0.1, 0.2, 0.3$ moving from left to right and top to bottom.

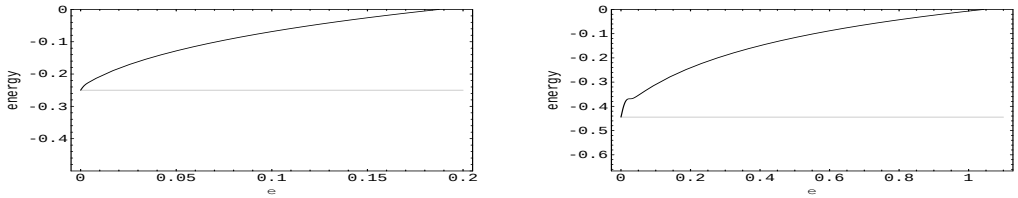

Figure 5.8: Plots of energy versus ϵ for system (5.20) with initial conditions $x(0) = 0, y(0) = 1, \dot{x}(0) = -1$ and $\dot{y}(0) = 1/\sqrt{2}$ for the left panel and $x(0) = 0, y(0) = 1, \dot{x}(0) = -3/4$ and $\dot{y}(0) = \sqrt{79}/12$ for the right panel. The time for both simulations is one full period of the unperturbed system with identical initial conditions.

imum time for each simulation is the period of the unperturbed periodic orbit of system (5.19) with the same initial conditions. It is clear from the simulations that the maximum energy gain does not necessarily occur at maximum time. In fact, for ϵ large enough, the excitation will force the orbit outside of the periodic regime, that is the negative energy regime. If the excitation were removed once the orbit leaves the periodic regime and the unperturbed system integrated further, the resulting orbit would be unbounded.

The plots shown in Fig. 5.8 show energy versus ϵ for system (5.20) with initial conditions in the periodic regime and integrated forward in time for one period of system (5.19) with identical initial conditions. In both simulations, the energy gen-

erally increases as ϵ increases.

5.10 Conclusion

The hope is that an unknown system in periodic or nearly periodic motion can be excited to higher energy levels using time-trace data recorded over one previous pseudo-period. This section explored the case of Classical Hamiltonian systems with internal damping and forcing with periodic or nearly periodic motion in a neighborhood of the initial conditions. The final results show that, while the theory is only proven for periodic Classical Hamiltonian motion, the method is generally quite effective at inducing energy increases in systems in nearly periodic motion with internal forcing and damping terms present. Of course, the more difficult question is finding a method to implement this algorithm in an unknown system. The placement of the forcing term on the right side of equation (5.8) is crucial. The mechanism for implementing the forcing function in this manner for a realistic system is a problem for further study.

References

[1] Bayly, P. V. and L. N. Virgin, 'An Experimental Study of an impacting pendulum.' *Journal of Sound and Vibration*, **164**, (2) 1993, 363–374.

[2] Bayly, P. V., 'On the Spectral Signature of Weakly Bilinear Oscillators.' *Journal of Vibration and Acoustics*, **118**, 1996, 353–361.

[3] C. Chicone, *Ordinary Differential Equations with Applications*, 2nd Ed. (New York: Springer-Verlag), 2006.

[4] C. Chicone and M. Jacobs, Bifurcation of critical periods for plane vector fields, *Transactions of the American Mathematical Society*, **312** (2) 1989, 433–486.

[5] R. Chouikha and F. Cuvelier, Remarks on some monotonicity conditions for the period function, *Appl. Math.* (Warsaw), **26** (3) 1999, 243–252.

[6] S.-N. Chow and Duo Wang, On the monotonicity of the period function of some second order equations, *Časopis Pěst. Mat.*, **111** (1) 1986, 14–25.

[7] J.-P. Françoise, The successive derivatives of the period function of a plane vector field, *J. Differential Equations*, **146** (2) 1998, 320–335.

[8] E. Freire, A. Gasull and A. Guillamon, First derivative of the period function with applications, *J. Differential Equations* **204** (1) 2004, 139–162.

[9] W. Goldsmith, *Impact*, (London: Edward Arnold), 1960.

[10] Guckenheimer, J. and P. Holmes, *Nonlinear Oscillations, Dynamical Systems, and Bifurcation of Vector Fields*, 2nd Ed. (New York: Springer-Verlag), 1986.

[11] Hertz, H., 'On the elastic contact of solids.' *Journal für die reine und angewandte Mathematik* **92**, 1881, 156–171.

[12] Hunt, K. H. and F. R. E. Crossley, 'Coefficient of restitution interpreted as damping in vibroimpact.' *Journal of Applied Mechanics*, **97**, 1975, 440–445.

[13] Johnson, K. L., *Contact Mechanics*, Cambridge University Press, Cambridge, UK, 1985.

[14] Kandangath, A. Krishnamoorthy, S., Lai, Y., and Gaudet, J.A., 'Inducing Chaos in Electronic Circuits by Resonant Perturbations' *IEEE Transactions on Circuits and Systems* **54**, (5) 2007, 1109–1119.

[15] Ladislav, P. and F. Paterka, 'Impact Oscillator with Hertz's Model of Contact.' *Meccanica* **38**, 2003, 99–114.

[16] H. Lichardová, The Period of a Whirling Pendulum, *Mathematica Bohemica*, **126** (3) 2001, 593–606.

[17] Mann, B. P., Garg, N. K., Young, K. A., and A. M. Helvey, 'Milling bifurcations from structural asymmetry and nonlinear regeneration.' *Nonlinear Dynamics*, **42**, 2005, 319–337.

[18] Mann, B. P. and M. A. Koplow, 'Symmetry breaking bifurcations in a parametrically excited pendulum.' *Nonlinear Dynamics*, **46**, (4) 2006, 427–437.

[19] Mann B. P., R. E. Carter, and S. S. Hazra, 'Experimental study of an impact oscillator with viscoelastic and Hertzian contact.' *Nonlinear Dynamics*, **50** (3) 2007, 587–596.

[20] Moore, D. B. and S. W. Shaw, 'The experimental response of an impacting pendulum system.' *International Journal of Non-Linear Mechanics*, **25**, 1990, 1–16.

[21] Nordmark, A. B., 'Non-periodic motion caused by grazing incidence in an impact oscillator.' *Journal of Sound and Vibration* **145**, (2) 1991, 279–287.

[22] Quinn, D. D., 'Finite duration impacts with external forces.' *Journal of Applied Mechanics*, **72**, 2005, 778–784.

[23] F. Rothe, The energy-period function and perturbations of Hamiltonian systems in the plane. *Oscillations, bifurcation and chaos* (Toronto, Ont., 1986), 621–635, CMS Conf. Proc., 8, Amer. Math. Soc., Providence, RI, 1987.

[24] Shaw, S. W. and P. J. Holmes, 'A periodically forced piecewise linear oscillator.' *Journal of Sound and Vibration*, **90**, 1983, 129–155.

[25] Slade, K. N., Virgin, L. N., and P. V. Bayly, 'Extracting information from interimpact intervals in a mechanical oscillator.' *Physical Review E*, **56**, (3) 1997, 3705–3708.

[26] Wiercigroch, M. and B. Kraker, *Applied Nonlinear Dynamics and Chaos of Mechanical Systems with Discontinuities*, Cambridge University Press, Cambridge, UK, 2000.

[27] Wiggins S., *Introduction to Applied Nonlinear Dynamical Systems and Chaos*, 2nd Ed. (New York: Springer-Verlag), 2003.

[28] Zeebroeck, M. V., Tijskens, E., Liedekerke, P. V., Deli, V., Baerdemaeker, J. D., and H. Ramon, 'Determination of the dynamical behavior of biological materials during impact using a pendulum device.' *Journal of Sound and Vibration*, **266**, 2003, 465–480.

[29] A.A. Zevin and M.A. Pinsky, Monotonicity criteria for an energy-period function in planar Hamiltonian systems, *Nonlinearity* **14** (6) 2001, 1425–1432.

VITA

K.R. Felts was born May 16th, 1978 in Poplar Bluff, Missouri. In 1996 he graduated from Poplar Bluff High School. He continued his education at the University of Missouri, where he graduated with a BS in Mathematics in 2001. He then began his graduate work at the University of Missouri, completing a MS in Mathematics in 2003. He was married to Kathy Schmidtke in 2007 and his son, Pierce Richard, was born in 2008. Also in 2008, he accepted a faculty position in the Computer Science and Mathematics Department at Columbia College.